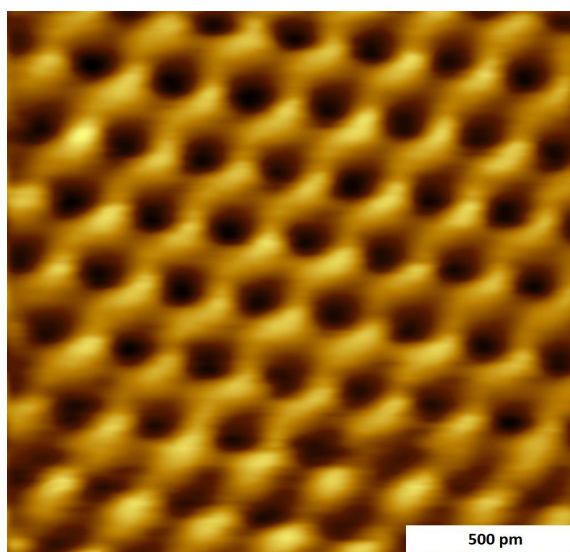


**Study of Electronic and Magnetic Properties
of Cobalt Nanoclusters on Graphite**



Master Thesis Report

Lucky Leonardus

MSc Nanotechnology

University of Twente, the Netherlands

Aug, 2010

NANO ELECTRONICS.

This master thesis work was performed at:

NanoElectronics & Physical Aspect of Nanoelectronics

University of Twente

Drienerlolaan 5

7522 NB Enschede

The Netherlands

The MSc committee consists of:

Prof. dr. ir. W. G. van der Wiel

Prof. dr. ir. H. J. W. Zandvliet

dr. ir. M. P. de Jong

dr. P. K. J. Wong

List of Abbreviations

Anisotropic magnetoresistance	(AMR)
Cobalt	(Co)
Current in plane	(CIP)
Current perpendicular to the plane	(CPP)
Current parallel/anti-parallel magnetization	(I_P / I_{AP})
Conductance of majority/minority spins electrons	(G_{Maj} / G_{Min})
Density of states	(DOS)
Ferromagnetic	(FM)
Giant Magnetoresistance	(GMR)
Graphene layers	(Gr)
Highly ordered pyrolytic graphite	(HOPG)
Hard disk drive	(HDD)
Insulating layer	(I)
Magnetic tunnel junction	(MTJ)
Magnetic random access memory	(MRAM)
Nonmagnetic layer	(NM)
Magnetoresistance parallel/anti-parallel magnetization	(R_P / R_{AP})
Number of majority/minority spins electrons per unit volume	(N_{Maj} / N_{Min})
Right/Left circular photons	(RCP / LCP)
Scanning tunneling microscopy	(STM)
Scanning tunneling spectroscopy	(STS)
Transition metals	(TM)
Tunneling magnetoresistance	(TMR)
Ultra-high vacuum	(UHV)
Vibrating sample magnetometer	(VSM)
X-Ray magnetic circular dichroism	(XMCD)

Abstract

We investigated the combination of cobalt (Co) and highly ordered pyrolytic graphite (HOPG) for spintronic applications. We deposited Co on HOPG in UHV to study its growth, and to characterize the interfacial electronic and magnetic properties. In our study, we remained in the nucleation-dominated regime with Co coverage below 5%, as characterized by scanning tunneling microscopy (STM). We observed individual Co ad-atoms initially sitting at the β -sites of the graphite surface lattice, and subsequently filling the other sites to form nanoclusters. The Co nanoclusters growth was found to follow the Volmer-Weber mode, independent of deposition time. The mean diameter and height of the isolated nanoclusters are 3.4 ± 0.2 nm and 0.49 ± 0.045 nm respectively. The aspect ratio of the nanoclusters, defined as height divided by diameter (h/d), is ~ 0.15 .

I - z scanning tunneling spectroscopy (STS) measurements, recorded with various applied bias voltages and a fixed current set-point of 1 nA, were taken at room temperature. For bare graphite samples, these data measurements later were interpreted as a mapping of the inverse decay length (κ) which represents electronic tunneling properties of the tip-graphite system at low bias range (near Fermi level). From spatial mapping of the inverse decay length, with a maximum value of 2.46 nm^{-1} at -0.5 V, it was shown that the tunneling current into the graphite was carried by electrons with a much lower parallel wave vector $k_{||}$ value than $k_{||} = K$ points = 17 nm^{-1} (from -0.5 V to 0.5 V).

After Co deposition, I - V STS data, using various various applied bias voltages and current set-points, were taken both at room temperature and at 95 K, to study the electronic properties of the Co nanoclusters. It turned out, however, that it is not possible to distinguish the Co nanoclusters from the HOPG substrate, mainly due to their similar *conductivity*¹ behavior.

To probe the magnetic and electronic properties of the nanoclusters, we also performed X-ray magnetic circular dichroism (XMCD) at 77 K. It is known that oxygen contaminants and defects on the graphite surface, as well as minute residual gases even in UHV, have a profound influence on the electronic and magnetic properties of Co nanoclusters. The measurements showed that the adsorbed Co clusters on HOPG were metallic, as evidenced by the lack of multiplet structure at the Co $L_{2,3}$ edges in the measured spectra. Other magnetic properties characterization was done using a vibrating sample magnetometer (VSM), to investigate the magnetization of the Co nanoclusters. Both measurements indicated paramagnetic behavior of the Co nanoclusters.

¹ Both Co and graphite are conductors. Just like any metal, Co is conducting due to overlap electronic bands structure at Fermi level. Graphite is defined as semimetal has electronic bands structure that only crossed at the K points at the Fermi level.

Table of Contents

1. Introduction	1
1.1. Motivation	1
1.2. Outline	1
2. Theoretical Background	2
2.1. Spintronics	2
2.2. Giant Magnetoresistance (GMR)	2
2.3. Tunneling Magnetoresistance (TMR)	4
2.4. Spin Filters	7
2.5. Graphene and Graphite as Spin Filters	9
3. Experimental Setup	12
3.1. Scanning Tunneling Microscopy/Spectroscopy (STM/STS)	12
3.2. X Ray Magnetic Circular Dichroism (XMCD)	13
3.3. Vibrating Sample Magnetometer (VSM)	15
4. Results and Discussions	16
4.1. The Inverse Decay Length Measurement	16
4.2. STM/STS Cobalt Nanoclusters on HOPG	18
4.2.1 Morphology Study	18
4.2.2 Electronic Properties Study	24
4.3. XMCD Cobalt Nanoclusters	25
4.4. VSM Measurement	26
5. Conclusions and Recommendations	27
5.1. Conclusions	27
5.2. Recommendations	27
6. Acknowledgments	29
7. References	30
8. Appendix A – Spatial Mapping of Inverse Decay Length	32

1. Introduction

1.1. Motivation

Graphite and especially graphene (single layers of sp^2 -hybridized carbon from which graphite is built) have attracted broad interest in the scientific community. That is because of their exciting physical properties, which are mainly derived from the fact that they have zero band gap energy at the Fermi K points. At these K points, also known as Dirac points, the energy E versus wave-number k is linear for energies close to Fermi energy E_F . It follows Dirac equation for mass-less particles, thus leads to very high carrier mobility. The intrinsic mobility of graphene at room temperature can be as high as $200,000 \text{ cm}^2\text{V}^{-1}\text{s}^{-1}$.

Spintronics as part of nanoelectronics also emphasizes active usage and manipulation of carrier spins in carbon-based materials. Such materials hold strong promise as spin transport media because of their potentially weak hyperfine and spin-orbit interactions, thus resulting in long spin lifetimes ($\tau_s \sim 10^{-5}$ - 10^{-7} s as compared with $\sim 10^{-10}$ s in metals) [1]. The longer the spin lifetimes in the systems, the bigger the possibility for the electrons to propagate without losing their spin orientation. Several theoretical studies suggested to use graphene/graphite (Gr) in combination with transition metal (TM) ferromagnets (FM) for spin filter devices [2-3]. Theoretically, it is possible to have perfect spin filtering in a device, where several graphene layers are sandwiched between two FM electrodes. That is because of the following reasons, which are: conservation of wave-vector k for transport in epitaxial structures; finite density of states (DOS) of graphite at the K points, such that electrons that cross a FM|Gr|FM structure will mostly reside at the K points; and the FMs considered have only the minority spin electrons (N_{Min}) at the K points.

In this project, an effort has been made to investigate the electronic and magnetic properties of ferromagnetic Co on HOPG substrate. The Co was deposited in the evaporation chamber integrated with a variable temperature UHV STM. As known from earlier studies, Co grows on HOPG as clusters. Since our investigation focuses at low-coverage Co, the Co clusters are predicted to have a size of only a few nm. The topography and electronic properties of the nanoclusters hence can be studied by STM/STS. Meanwhile, by depositing a capping layer to prevent Co oxidation, the sample can be characterized ex-situ with XMCD and VSM for extracting its magnetic properties.

1.2. Outline

This section shortly describes the outline of this thesis. At first the relevant theoretical background will be discussed in Chapter 2. Treated here are a brief discussion of spintronics and its underlying physics (section 2.1), the GMR effect that gave birth to spintronics research (section 2.2), the experimental work of magnetic tunnel junction (MTJ) devices (section 2.3), the spin filter effect for injecting spins and improving magnetoresistance effect (section 2.4) and the theoretical suggestion of integrating Gr layers as spin filters in MTJ-like structures (section 2.5). Chapter 3 deals with the experimental setup and methods, mainly covering scanning tunneling microscopy/spectroscopy (STM/STS), X-ray magnetic circular dichroism (XMCD), and vibrating sample magnetometer (VSM) instruments. In section 3.1, the STM is used to study electronic properties of the system, by means of I - z and I - V spectroscopy, and to investigate the growth of Co on the HOPG. After this, two characterization techniques often used for magnetic properties are described, XMCD in section 3.2 and VSM in section 3.3. The main results will be presented in Chapter 4. In this chapter, we will also discuss experimental problems that were encountered. Finally, we draw conclusions and give recommendations in Chapter 5 and Chapter 6, respectively.

2. Theoretical Background

2.1. Spintronics

A hard disk drive (HDD) is a non-volatile storage device for digital data. The technology development in HDDs has been changing at a fast rate. Since the first hard disk drive (HDD), that was built in 1956, the areal bit-density has increased enormously - from 2 kbit in⁻² to 421 Gbit in⁻². This areal density improvement results in smaller, lighter, and faster data storage, while at the same time maintaining a competitive price. One of the most important developments that triggered a particularly strong areal density increase, especially between 1991 and 2003, is due to the discovery of the giant magnetoresistance (GMR) effect [4].

Historically, magnetoresistance, i.e. a resistance that depends on the magnetization direction in a magnetic conductor, had been discovered in 1856 by William Thomson. This effect is now known as anisotropic magnetoresistance (AMR), which is very relatively small in amplitude ($\Delta R/R \approx 1\%$). Later in 1988-1989, the GMR effect was discovered by two independent groups (Albert Fert *et al.* in France and Peter Grünberg *et al.* in Germany) [5-6]. This discovery was practically applicable in 1991 when IBM introduced GMR read-heads combined with a ring element for writing (see Fig. 1). These systems are based on a longitudinal recording system where magnetization is applied in plane of the disk. The read element works by sensing the stray magnetic field from the transition between magnetic domains [4].

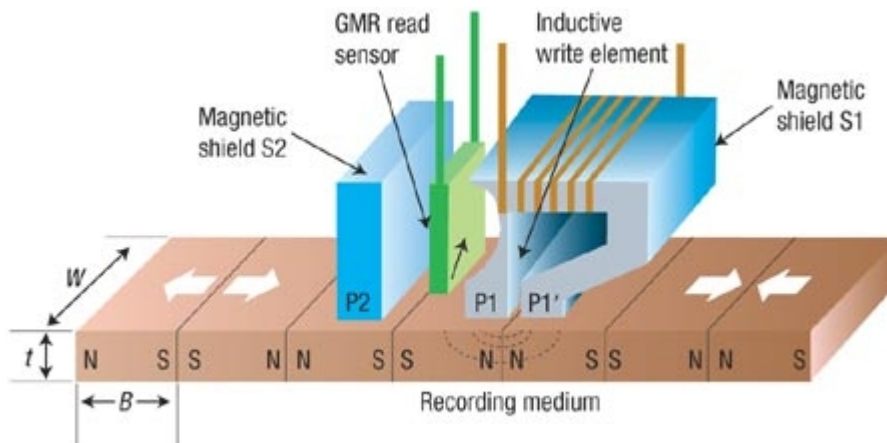


Figure 1. Schematic illustration of a longitudinal recording system introduced by IBM for its HDD in 1991. The distances P1-P1' and P1-P2 between the pole pieces of the magnetic shield S1 and S2 define respectively the 'write' and 'read' gaps. This gap depends on the minimum length B of the magnetic domain. W is the track width and t is the thickness. In a perpendicular recording system nowadays, W and B are around 100 nm and 30 nm respectively [7].

The discovery of GMR was a technological leap at that time. A strong research effort directed to obtain even higher MR was initiated, and the sensitivity and signal to noise ratio of GMR greatly improved. Since then, the research direction that originated from GMR research is known as spintronics (acronym of SPIN ELECTRONICS) or magnetoelectronics.

2.2. Giant Magnetoresistance (GMR)

In ferromagnetic materials, one can distinguish two projections of spins electrons: the majority spin electrons with magnetic moments parallel to the magnetization, and the minority spin electrons with magnetic moments anti-parallel to the magnetization. Then, the magnetization M of a ferromagnetic material is defined by the difference between the number of majority spin electrons per unit volume (N_{Maj})

and the number of minority spin electrons per unit volume (N_{Min}). For the sake of argument, we will label the spin orientation of the majority spins electrons as spin "up" and the minority spins electrons as spin "down".

The magnetic moment μ_s is defined as

$$\mu_s = -g_s \mu_B \left(\frac{S}{\hbar} \right) , \quad (1)$$

where g_s is the gyromagnetic ratio, μ_B is the Bohr magneton, S is electron spin, and \hbar is reduced Planck constant. Due to the negative constant of the gyromagnetic ratio, the magnetic moment is anti-parallel to the spin. Hence, the magnetic moment of spin up and spin down are anti-parallel and parallel with magnetization, respectively.

The theory of spin-polarized transport was first explained by Mott, with his two-current model [8]. In this model, the electrons of majority spins and the electrons of minority spins do not mix in the scattering processes. The conductivity (or resistivity) can then be expressed in terms of two independent and unequal parts for two different spin projections. The principle is depicted in Fig. 2 for the simplest case of a sandwich structure ferromagnetic (FM)|nonmagnetic metal (NM)|ferromagnetic (FM). When the two FM electrodes are magnetized parallel (P), only the spin up electron, which has opposite magnetization, will be scattered in FM electrodes, hence resulting in a low resistance. On the other hand, if two FM electrodes in the anti-parallel (AP) case, both spin up and spin down will be scattered in one FM electrode or the other, hence giving an increase in resistance (see Fig. 2A-B).

Besides the bulk effect, when the current is perpendicular to the plane (CPP configuration), the GMR effect is mainly induced by spin dependent scattering at the interface (see Fig. 2C-D). When the two FM electrodes are magnetized parallel (P), the spin up can travel through the sandwich structure almost unscattered, hence resulting in low resistance. On the other hand, if two FM electrodes in the anti-parallel (AP) case, both spin up and spin down will be scattered in one FM electrode or the other, hence giving an increase in resistance [7]. For this discovery, A. Fert and P. Grünberg were awarded the Nobel prize in physics 2007.

The GMR ratio is defined as

$$GMR = \frac{(\alpha - 1)^2}{4\alpha} ; \quad \alpha = \frac{R_{Maj}}{R_{Min}} , \quad (2)$$

where R_{Maj} and R_{Min} are the resistances of the majority spin electron and the minority spin electrons, respectively.

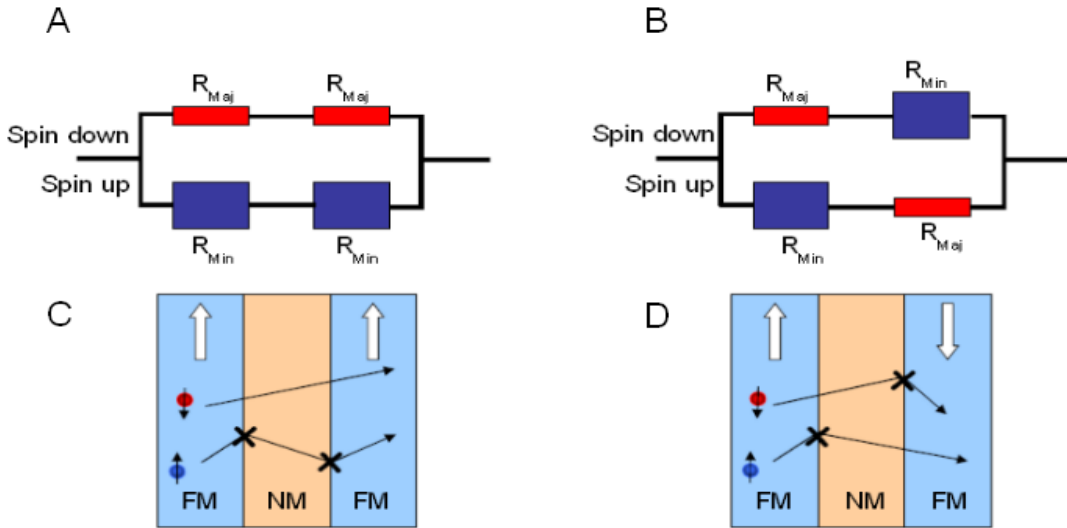


Figure 2. (A, B) Schematic illustrations of the spin-valve GMR effect: (A-B) The two-current model of GMR where R_{Maj} (red box) and R_{Min} (blue box) are connected in: (A) P magnetization, (B) AP magnetization. (C-D) Spin dependent scattering at the interface for: © In P magnetization, the spin up which has opposite magnetization can travel from through the NM spacer almost unscattered, resulting in low MR. (D) In AP magnetization, both spin up and spin down are scattered in one FM electrode or the other, resulting high MR.

In this type of structures, based on a nonmagnetic metal interlayer, the maximum GMR achievable by engineering the various layers and interfaces in the stacks has reached a saturation point, meaning that the progress in obtaining higher GMR has been very little for a long period of time [9]. In an alternative configuration, the nonmagnetic metal layer is replaced by an insulating barrier of a few nanometers thickness, such that electrons can tunnel from one electrode to the other through the insulating barrier. A structure based on this principle is known as a magnetic tunnel junction (MTJ). Here, instead of diffusive scattering across the metal (conductive) interlayer as in GMR structures, quantum mechanical tunneling determines the current. In the following section, the operation principle of an MTJ is explained in detail.

2.3. Tunneling Magnetoresistance (TMR)

As mentioned above, an MTJ consists of two ferromagnetic electrodes separated by an insulating barrier of a few nanometers. From quantum mechanics, it is known that when a voltage is applied across two metal electrodes separated by a thin barrier, the wave properties of the electrons may enable them to be transmitted across the barrier. A current then sets in due to this quantum tunneling effect. In quantum mechanics, this tunneling current I depends exponentially on barrier height and thickness of the barrier. But, in the MTJ, this tunneling current also depends on the relative orientation of magnetizations of the two FM electrodes.

The first TMR experiment had been done by M. Jullière in 1975 with a Fe|Ge (100-150 Å)|Co MTJ at 4.2 K [10]. Although the MR effect was low (14%) even at low temperature, still this experiment proved that the changes in conductance/resistance on the junction were indeed related to the spin dependent transport, as controlled by the relative magnetization of the electrodes.

The TMR effect also can be explained with a two-current model analogous to that proposed by Mott. Jullière assumed that the tunneling current is spin polarized with contributions from the N_{Maj} and N_{Min} , and that during tunneling the spin orientation of electrons will not change. In Jullière's model, the tunneling current is taken to be proportional to the density of states (DOS). Conductance changes between P and AP magnetization is illustrated in Fig. 3, which shows a sandwich structure of an FM||FM MTJ device. This

sandwich structure, comprising ferromagnetic (FM)|Insulator (I)|ferromagnetic (FM), is usually defined also as a pseudo spin valve. When bias voltage is applied to both FM electrodes, the electrons will tunnel across the non-magnetic insulating barrier, e.g. Al₂O₃ or MgO. Using the assumption of spin conservation during tunneling, the spin up electrons at one FM will fill the empty spin up electron states at the other FM. The same applies to spin down electrons. The total current (at zero bias voltage) corresponding to a parallel I_P and anti-parallel I_{AP} magnetization can be estimated as

$$I_P \propto (T^\uparrow \times \rho_1^\uparrow \times \rho_2^\uparrow) + (T^\downarrow \times \rho_1^\downarrow \times \rho_2^\downarrow) , \quad (3)$$

$$I_{AP} \propto (T^\uparrow \times \rho_1^\uparrow \times \rho_2^\downarrow) + (T^\downarrow \times \rho_1^\downarrow \times \rho_2^\uparrow) , \quad (4)$$

where $\rho_{1,2}^{\uparrow,\downarrow}$ are the DOS of spin up and spin down electrons at the Fermi level in the first (FM1) and second (FM2) electrodes. $T^{\uparrow,\downarrow}$ are the tunneling probabilities for majority (spin up) and minority (spin down) spins electrons.

Since the tunneling current is the product of the DOS, if one magnetize two identical FM electrodes, the tunneling current in AP will be smaller than in P. That because in P magnetization the channel connects large filled DOS and large empty DOS (see Fig. 3A), hence giving an increase in tunneling current from the minority (spin down) electrons contribution. While in AP magnetization, the product of the DOS of FM1 and FM2 contains a large and small number, hence resulting in lower tunneling current contributed equally from both spin projections (see Fig. 3B).

The TMR ratio can be expressed in terms of changes in the resistance or conductance, and in terms of the spin polarization P at the Fermi level of the FM layers.

$$TMR = \frac{(R_{AP} - R_P)}{R_P} = \frac{(G_P - G_{AP})}{G_{AP}} = \frac{(2P_1 P_2)}{(1 - P_1 P_2)} , \quad (5)$$

$$P_{1,2} = \frac{(N_{Maj} \times T^\uparrow - N_{Min} \times T^\downarrow)}{(N_{Maj} \times T^\uparrow + N_{Min} \times T^\downarrow)} , \quad (6)$$

where $R_{P,AP}$ and $G_{P,AP}$ are the resistance and conductance of the parallel and anti-parallel magnetization, respectively; $P_{1,2}$ are the spin tunnel polarizations of electrode 1 and 2; $N_{Maj,Min}$ is the total majority (spin up) and the minority (spin down) spin electrons DOS of both FM electrodes.

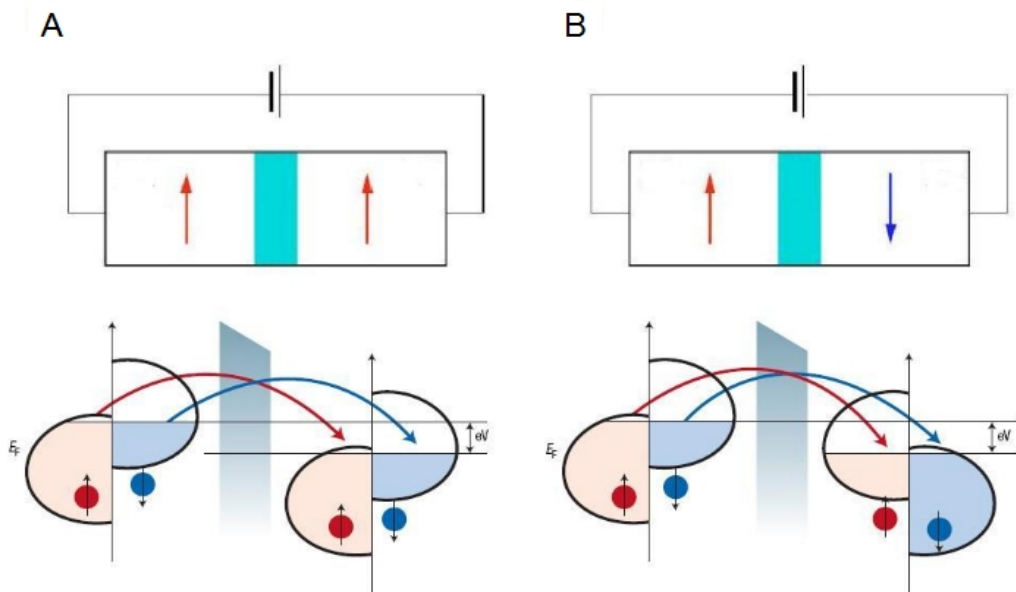


Figure 3. Schematic illustration of Jullière's model of the TMR phenomenon: (A) P magnetization (B) AP magnetization [7-8].

The aim of spintronics is to exploit spin effects in electronics at room temperature. The first breakthrough of TMR happened in 1995. The first room-temperature TMR was reported by two groups, Miyazaki and Tezuka [11] and Moodera, *et al* [12]. Since then, improvement of the Al_2O_3 tunnel barrier continued until Al_2O_3 -based MTJs reached 70% TMR at room temperature. This 70% TMR was close to the limit of Jullière's model, mainly because of limitation in electrodes polarization $P_{1,2} < 0.6$ (using Eq. 5 with $P_{1,2} = 0.6$, yields 112.5% TMR).

In order to obtain higher TMR, it was proposed to improve the tunnel barrier, such that during tunneling the spins are less scattered. The suggested tunneling process is known as coherent spin-dependent tunneling as predicted theoretically for an MTJ with a crystalline tunnel barrier of MgO (001) [13-14]. This coherent spin-dependent tunneling does not happen in an Al_2O_3 tunnel barrier since it is amorphous, and thus results in a nonsymmetrical structure (if the two interfaces are not the same) with smaller tunneling probabilities [15]. Several attempts to fabricate high quality MgO tunnel barriers finally succeeded in 2004. Yuasa, *et al.* [16] reported a giant TMR effect of 180% at room temperature in single-crystal Fe|MgO|Fe [16]. Until now, the development of MgO tunnel barriers for MTJ devices working at room temperature is still continuing as one can see from the trend in Fig. 4A.

In practical applications, using single-crystal Fe|MgO|Fe MTJs is not a viable solution, because a certain stacking structure is required (see Fig. 4B). Typically, practical MTJs consist of a seed layer, an antiferromagnetic (AF) layer, a synthetic ferrimagnetic structure (SyF) for the pinned layer, a tunnel barrier, and a ferromagnetic layer for the free layer. The MgO (001) barrier cannot be grown on the fcc(111)-oriented AF/SyF. It was found that by using amorphous CoFeB for the FM layers, an MgO (001) barrier can be grown as (001)-oriented polycrystalline, via crystallization of the CoFeB and MgO upon post-deposition annealing [15].

One of the highest TMR ratios obtained was 604% at room temperature using a thermally oxidized Si wafer | Ta(5 nm)|Ru(10 nm)| $\text{Co}_{20}\text{Fe}_{60}\text{B}_{20}$ (6 nm)|MgO(1.5 or 2.1 nm)| $\text{Co}_{20}\text{Fe}_{60}\text{B}_{20}$ (4 nm)|Ta(5)|Ru(5 nm) junction. This was achieved after annealing the MTJ at 525°C, which improved the MgO barrier quality in terms of suppressed Ta diffusion into the MTJ, improved the degree of the (001) orientation and relaxed the lattice constraint (see Fig. 4C).

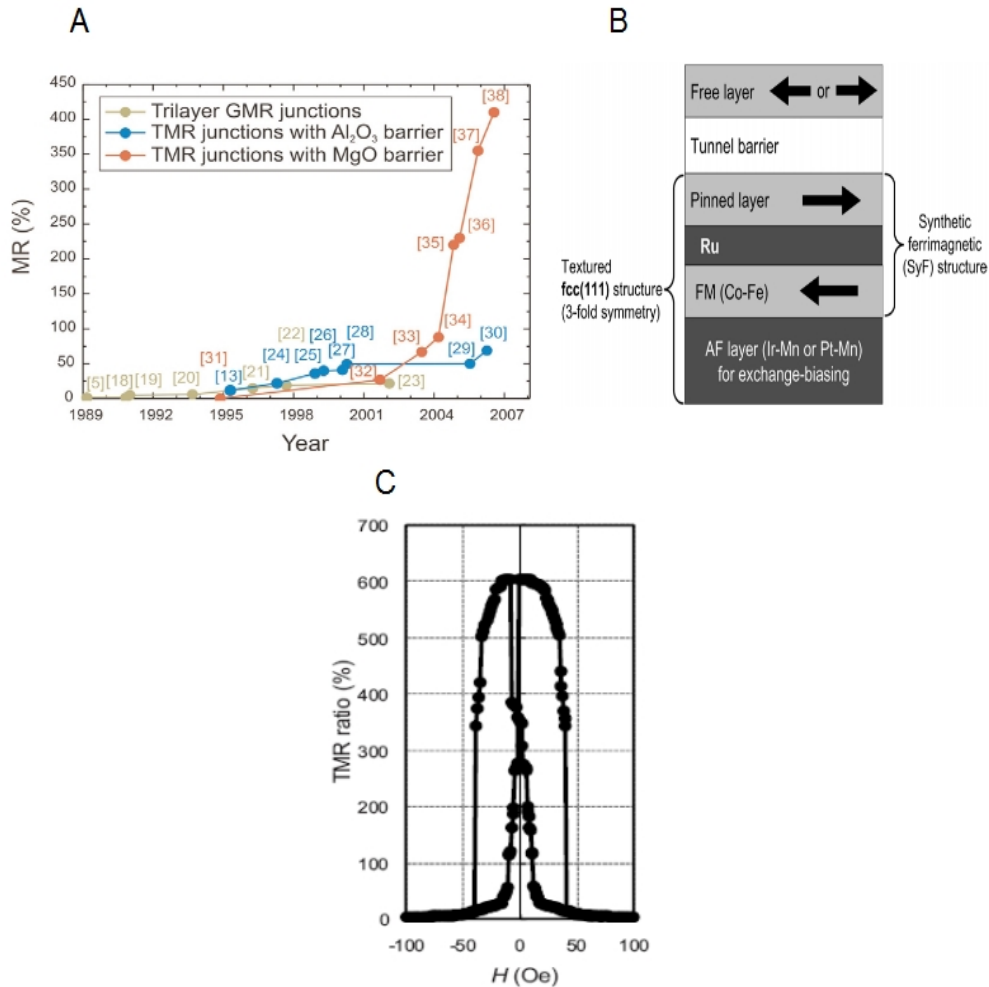


Figure 4. (A) Development of MR ratio at room temperature during the last decades [9]. (B) Schematic illustration of cross-sectional structure of a MTJ for practical application [15]. (C) Magnetoresistance loop of MTJ $\text{Co}_{20}\text{Fe}_{60}\text{B}_{20}(6 \text{ nm})|\text{MgO}(1.5 \text{ or } 2.1 \text{ nm})|\text{Co}_{20}\text{Fe}_{60}\text{B}_{20}(4 \text{ nm})$ annealed at 525°C [17].

2.4. Spin Filters

As mentioned above, one thing hindering the development of spintronics devices so far is the ability of the FM electrodes to produce almost 100% spin polarization current sources. According to Jullière's model (see Eq. 2), one easily can see that with higher polarization of the electrodes, higher TMR can be achieved. One way to achieve maximum TMR is by engineering or by replacing FM transition metal electrodes (such as, Co, Ni, and Fe) with other ferromagnetic materials that have a full spin polarization ($|P|=1$). There are peculiar types of ferromagnetic materials with $|P|=1$, so-called half metals, for example, CrO_2 , Co_2MnSi , Fe_3O_4 , and $\text{La}_{1-x}\text{Sr}_x\text{MnO}_3$. However, in practice these materials do not show $|P|=1$ at the interface so far. Another alternative for higher polarization is to combine the TMR effect with the spin filter effect (that done in MgO-based MTJs), where coherent tunneling induces k -vector selection and symmetry-dependent decay rates of electron wave functions [18-19].

The spin filter effect was discovered earlier than TMR. It was based on the experimental work by I. Giaever and L. Esaki for which they were awarded the Nobel prize in physics in 1973. In 1967, Esaki, *et al.* [20] showed that by sandwiching Eu chalcogenides (such as, EuSe and EuS) between Al and Au electrodes, changes in I - V curves were influenced by the applied magnetic field during tunneling. Also by applying a magnetic field, the tunnel barrier was lowered by 25% at 2K.

This experiment was refined with tunnel junctions Au(11-50 nm)|EuS(1.7,3.3, and 5 nm)|Al(4.2nm) by the MIT group headed by Moodera [21-22]. The semiconductor EuS has a Curie temperature T_c around 16.6-16.8 K which means that below this T_c , the EuS will become ferromagnetic. At temperatures higher than T_c , the barrier does not distinguish between spin up and spin down electrons. However, below T_c , the conduction band in EuS will have spin splitting $2\Delta E_{ex}$, hence the barrier height becomes spin dependent as illustrated in Fig. 5A. Then, one spin orientation has a much larger tunneling probability than the other due to different barrier height Φ_{\uparrow} for spin up and Φ_{\downarrow} for spin down [23]. By this phenomenon, one can expect the tunneling current to be spin-polarized almost perfectly. The spin filter effect can be shown by the tunneling conductance (dI/dV) measurement and the spin polarized tunneling can be indicated by the splitting of conductance with applied magnetic field (see Fig. 5B).

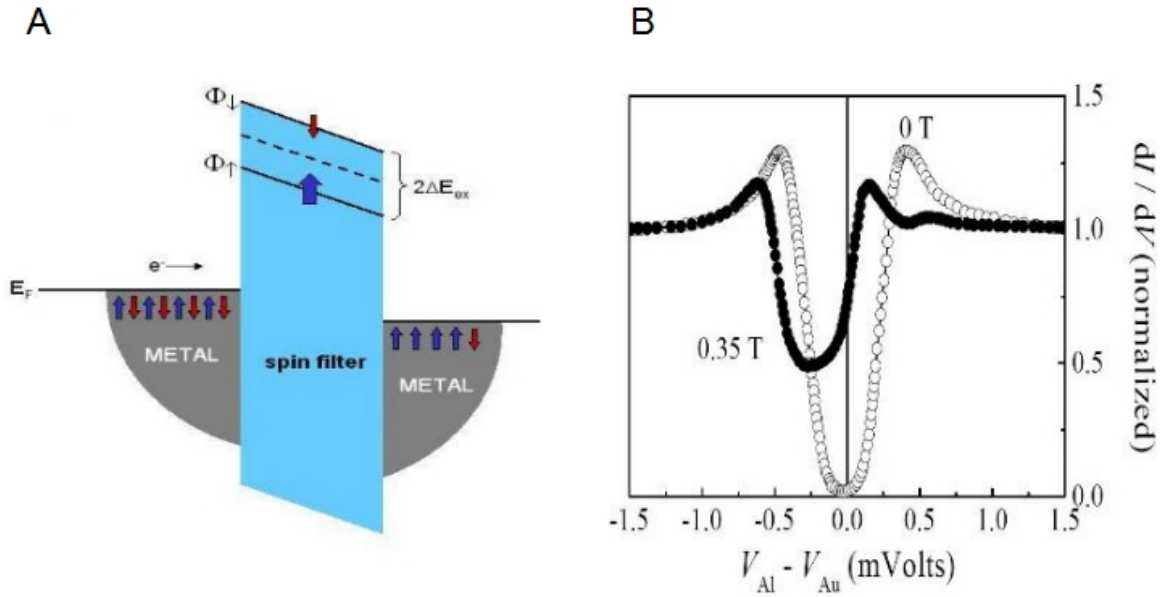


Figure 5. (A) Schematic illustration of spin filter effect on Eu chalcogenides. Below T_c , spin up electrons tunnel through the lower barrier while spin down tunnel through the higher barrier. As a result, the tunneling current will be spin polarized [23]. (B) Conductance (dI/dV) vs. Voltage (V) at $\mu_0 H = 0$ T and $\mu_0 H = 0.35$ T for measured at 0.4 K. It is shown that for 0.35 T the tunneling current caused mostly by majority spin conductance; gives a polarization $P \approx 80\%$ [22].

Since these demonstrations, variations of both the electrodes and the spin filter barrier have been investigated. For example, Moodera, *et al.* obtained almost 100% polarization with applied magnetic field $H \geq 1.2$ T on Ag|EuSe(antiferromagnetic)|Al at 0.45 K [24], and his team also investigated EuO as spin filter [25]. Until now, the pursuit of large spin filtering effects is continuing using various materials as tunnel barrier (see Table 1).

Material	Magnetic behavior	Tc (K)	Structure, a (nm)	Eg (eV)	$2\Delta E_{ex}$ (eV)	P (%)
EuO	Ferromagnetic	69.3	Fcc, 0.514	1.12	0.54	29
EuS	Ferromagnetic	16.6	Fcc, 0.596	1.65	0.36	86
EuSe	Anti ferromagnetic	4.6	Fcc, 0.619	1.8		100
BiMnO ₃	Ferromagnetic	105	Perovskite			22
NiFe ₂ O ₄	Ferrimagnetic	850	Spinel	1.2		22
CoFe ₂ O ₄	Ferrimagnetic	796	Spinel	0.57		

Table 1. Spin filter materials and their physical properties [23].

The first experiment that utilizes a spin filter effect to fabricate a MR tunnel device was demonstrated by LeClair, *et al.* in 2002 [18]. They observed an MR effect exceeding 100% on Si|SiO₂|Ta(5 nm)|Al(3 nm)|EuS(5 nm)|Gd(15 nm) tunnel junctions at 2K. This high MR indicates that the filtering efficiency was high (close to 100%) and this effect was named "spin filter injection magnetoresistance" (SFIM). Then it was realized that combination of both MR and spin filter effects in one tunnel junction was promising as a method for producing spin polarized current; useful for both memory application, and spin injection.

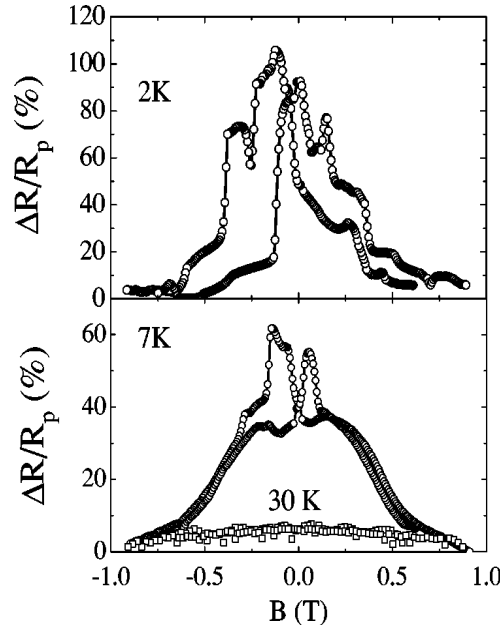


Figure 6. MR of Al|EuS|Gd junction as a function of applied magnetic field at 2 K (well below the EuS T_c); at 7 K; and at 30 K (well above the EuS T_c) [18].

2.5. Graphene and Graphite as Spin Filters

So far, it is expected that a spin filter MR junction should be working at room temperature. However, this effect is not observable at room temperature due to thermal disturbances. Recent experiment using CoFe₂O₄ tunnel barrier show still too small (TMR values -3% at 290 K) [26]. Therefore, several theoretical studies suggested a new spin filter based on graphene/graphite [2-3].

Using organic materials for MR devices was not really new. It is well known that organic materials have the potential of having longer spin relaxation times than metals ($\tau_s \sim 10^{-5}$ - 10^{-7} s as compared with $\sim 10^{-10}$ s in metals). Several experiments of MR devices using carbon nanotube as spacer have been conducted. However, still none of the devices give MR (nor a spin filter effect) at room temperature [1]. It was predicted that by using graphene or graphite as an intermediate layer between two transition metals (TM) ferromagnetic (FM) electrodes, perfect spin filtering can be achieved without being very sensitive to temperature [3].

The first main reason of the perfect spin filtering effect is because the lattice matching between graphene and TM (Co or Ni). In this case, the disorder becomes small. Compared to a lateral lattice mismatch of bcc-Fe|MgO and bcc-Co|MgO which are 3.8% and 2.8%, respectively [15, 27], the lattice mismatch for hcp-Co|Gr_(n) and fcc-Ni|Gr_(n) is 1.87% and 1.3%, respectively. The smaller the lattice mismatch, the smaller the number of structural defects caused by strain.

	Graphite	Co	Ni	Cu
a_{fcc} (Å) - expt		3.544	3.524	3.615
a_{hex} (Å) - expt	2.46	2.506	2.492	2.556
a_{hex} (Å) - LDA	2.45	2.42	2.42	2.49
d_{O} (Å)	3.32	2.04	2.03	3.18

Table 2. Lattice constants of Graphite, Co, Ni, and Cu (in Å). Equilibrium separation d_o is the separation for a graphene layer on top of graphite, Co, Ni, or Cu calculated within the DFT-LDA using in plane lattice constant 2.46 Å [2-3].

The second reason for using graphene is due to its distinctive electronic properties. It is known that graphene has only a finite DOS at E_F at the high-symmetry K points (also known as Dirac points) in the reciprocal space of the 2D Brillouin zones. At these K points, the energy and the momentum are conserved. This means that if transport occurs through the Gr from one TM layer to another TM layer, the conductance of majority electron spins (G_{Maj}) will be quenched and only the conductance of minority electron spins (G_{Min}) remains.

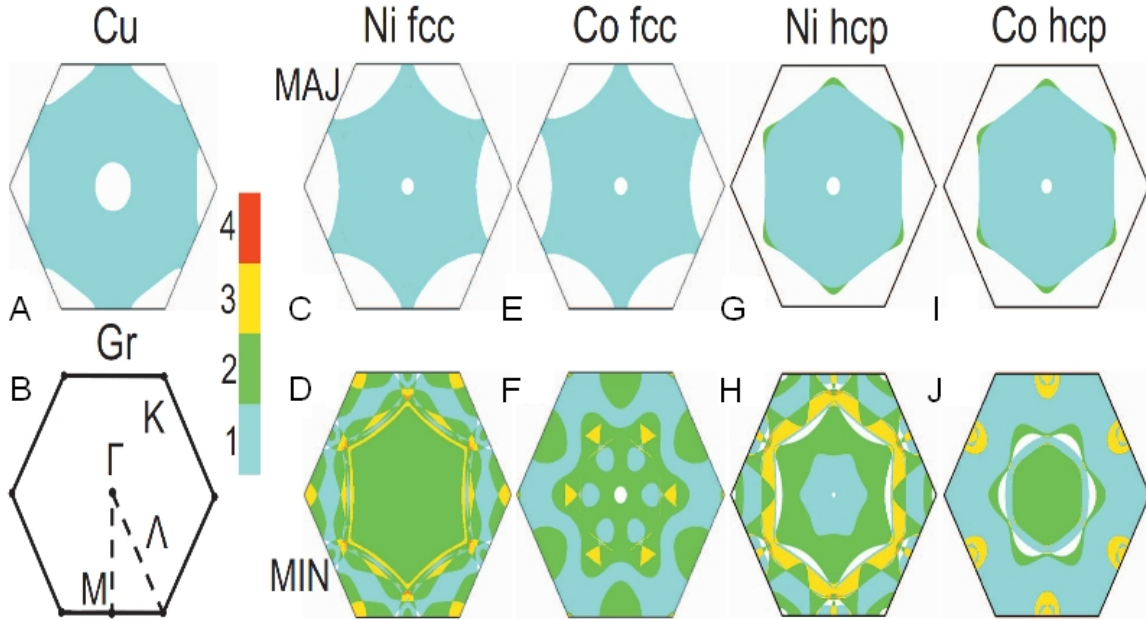


Figure 7. Projection of Fermi-surface for: (A) Fcc Cu. (B) Graphene and graphite. (C) Majority spin fcc Ni (111). (D) Minority spin fcc Ni (111). (E) Majority spin fcc Co (111). (F) Minority spin fcc Co (111). (G) Majority spin hcp Ni (0001). (H) Minority spin hcp Ni (0001). (I) Majority spin hcp Co (0001). (J) Minority spin hcp Co (0001). Color bar is indicating the number of Fermi-surface sheets [3].

Simulation of tunneling conductance was done for both CPP Ni|Gr_(n)|Ni and Co|Gr_(n)|Co, where n is the number of graphene monolayers (see Fig. 8). It was shown that in the AP configuration, the majority spins electrons will be filtered completely, hence resulting in spin polarized current by minority spins electrons.

Karpan, *et al.* showed by using the *pessimistic* definition of MR defined as [2-3]

$$MR = \frac{(R_{AP} - R_P)}{R_{AP}} = \frac{(G_P - G_{AP})}{G_P}, \quad (7)$$

the MR rapidly approaches 100%. Note that this 100% MR means that R_P is zero and implies that only

minority spins (spin down) contributed to the conductance. If one is using *optimistic* definition of MR (in Eq. 2), this means the MR will be very high – even one expect much higher MR ratio than 604% from Ref. [17]. Unwanted intermixing between Ni and Cu ($\text{Ni}_{50}\text{Cu}_{50}$ polycrystalline) only reduces the MR from 100% to 90%. Roughness and disorder effect were simulated to decrease the MR effect to be around 70%.

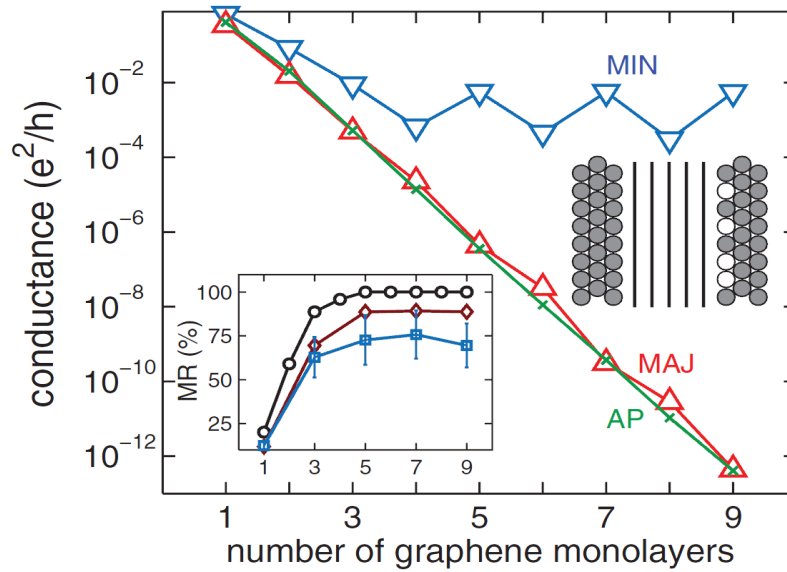


Figure 8. Conductance as a function of the number of graphene layers n for an ideal junction: ∇ = conductance for minority spins at parallel configuration; Δ = conductance for majority spins at parallel configuration; $/$ = conductance at anti parallel configuration. Inset: MR as a function of n for: o = ideal junction; \diamond = $\text{Ni}|\text{Gr}_{(n)}|\text{Cu}_{50}\text{Ni}_{50}|\text{Ni}$ junction; \square = roughness effect on one of the electrodes [2].

3. Experimental Setup

This project's aim is to prove experimentally whether the graphite or graphene as a spin filter is feasible. We used STM/STS as primary methodology for measuring electronic properties of the HOPG system, characterizing morphology after FM material (in this case Co) was deposited on the HOPG. For the study of magnetic properties, we used XMCD and VSM.

The experimental studies covered in this project are as follows:

1. With the I - z STS, one can measure the electronic properties near E_F of HOPG. Using the Simmons model, one can map the inverse decay length κ of the tunneling electrons at low bias voltages range (from -0.5 V to 0.5 V).
2. STM enables the study of the growth of Co onto HOPG. The electronic properties can also be studied using I - V STS measurement.
3. By depositing Al capping layer to prevent Co oxidation, the sample can be characterized ex-situ with XMCD and VSM for extracting its magnetic properties.

The details of experimental background and setup will be introduced in the next sections.

3.1. Scanning Tunneling Microscopy/Spectroscopy (STM/STS)

Scanning tunneling microscopy (STM) was invented by Binnig & Rohrer in 1982. They were awarded the Nobel Prize in Physics shortly afterward in 1986. In the STM, a metallic tip is brought so close to the surface so that the wave functions of tip and surface overlap each other. Then a bias voltage is applied and a tunneling current (in the range of nA) is generated. In general, when positive bias is applied on sample, the electrons tunnel from the tip to the empty states in the sample. For a negative bias it will be the opposite, the electrons tunnel from the occupied states from the sample to the tip. In the low bias range, the tunneling current can be approximated by :

$$I(V, z) \propto \frac{CV}{z} e^{(-2\kappa z)}, \quad (8)$$

where the C , κ , and z are a constant, the inverse decay length and the separation distance between tip and sample, respectively [28].

The STM technique with 0.1 nm lateral and 0.01 nm depth resolution; allows us to study the growth of epitaxial Co on HOPG. We used an RHK variable temperature UHV STM equipped with an electron beam evaporator. The deposition rate parameters were kept constant at 1 kV, filament current 7 A, and flux current 5 nA. However, we were varying the deposition time to obtain different coverages. The instrument setup can be seen below.

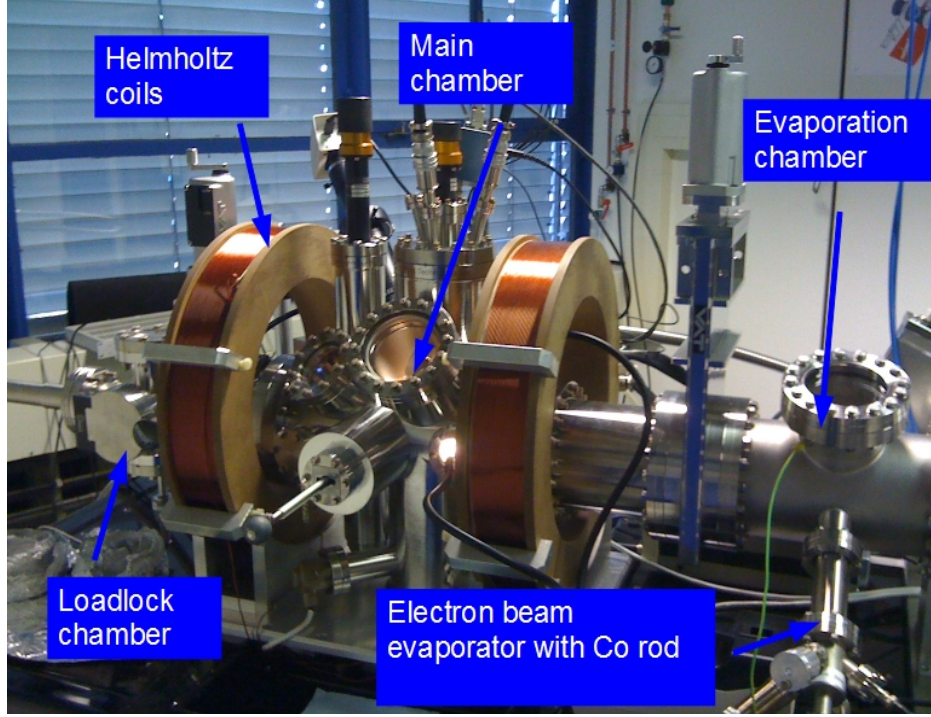


Figure 9. Experimental setup Variable Temperature UHV STM.

3. 2. X Ray Magnetic Circular Dichroism (XMCD)

Anisotropy phenomena of the charge density, the spin density, and the orbital moment of transition metal sandwiches can be studied by XMCD. The XMCD senses those local anisotropies around an atom that is excited by the absorption of polarized X-rays. XMCD offers superiority compared to other techniques because of specificity and sensitivity to core levels and thus the corresponding elements, and can probe quantitatively and separately spin and orbital magnetic moments and their anisotropies.

Magnetism in $3d$ transition metals arises because of exchange interaction between neighboring electrons. Each of these electrons has magnetic moment contributed from the spin moment m_s and the orbital moment m_o . Typically, the orbital moment is much smaller than spin magnetic moment. For example, the m_s and m_o for Co are $1.64\mu_B$ and $0.14\mu_B$. The magnetic properties of $3d$ -electrons are the best probed in an X-ray absorption experiment by excitation of $2p$ core electrons to unfilled $3d$ states (L -edge absorption spectra) [29].

The XMCD technique was pioneered by Schütz, *et al.* in 1987 [30]. They showed that the changes of X-ray absorption cross section depends on the direction of polarized X-rays (left and right) and are proportional to the spin polarization of the DOS. The proportionality between X-ray absorption (I_{XAS}) and the DOS (ρ), can be written as below formula:

$$I_{MCD} \equiv \frac{(I_{XAS}^L - I_{XAS}^R)}{(I_{XAS}^L + I_{XAS}^R)} = P_e \frac{(\rho_+ - \rho_-)}{(\rho_+ + \rho_-)}, \quad (9)$$

where $I^{L,R}$ are left and right polarized x-rays respectively; ρ_+ and ρ_- are spin up and spin down DOS; and P_e is the Fano factor which is related to a core hole spin-orbit coupling.

The basic principle of XMCD can be explained by the one-electron picture in Fig. 10. The right or left circularly polarized photons are used to transfer their angular momentum to the excited photoelectrons. Due to the spin-orbit coupling, at the ground state there are splitting of parallel ($p_{3/2}$) and anti-parallel ($p_{1/2}$)

spin- and orbital angular momentum. The $p_{3/2}$ level has X-ray absorption spectra at L_3 edge and the $p_{1/2}$ level has it at L_2 edge. The L -edge X-ray absorption spectrum is mainly dominated by deep core $2p \rightarrow$ empty $3d$ transitions. Right circular photons (RCP) transfer the opposite angular momentum to the electrons as left circular photons (LCP), and photoelectrons with opposite spins are excited in the two cases. The spins orientations (spin "up" and spin "down") is defined relative to the photon helicity.

In electric dipole transitions, spin flips are forbidden. Thus the spin up (or spin down) photoelectrons from the core $2p$ shell can only be excited into the spin up (or spin down) states in the empty $3d$ -band. The transition intensity of L -edge spectra therefore is proportional to the number of empty $3d$ states of a given spin. Since the quantization axis of the valence shell "detector" is given by the magnetization direction, the dichroism effect (intensity of L_3 and L_2 edges) is maximum if the photon spin direction and the magnetization directions are parallel and anti-parallel.

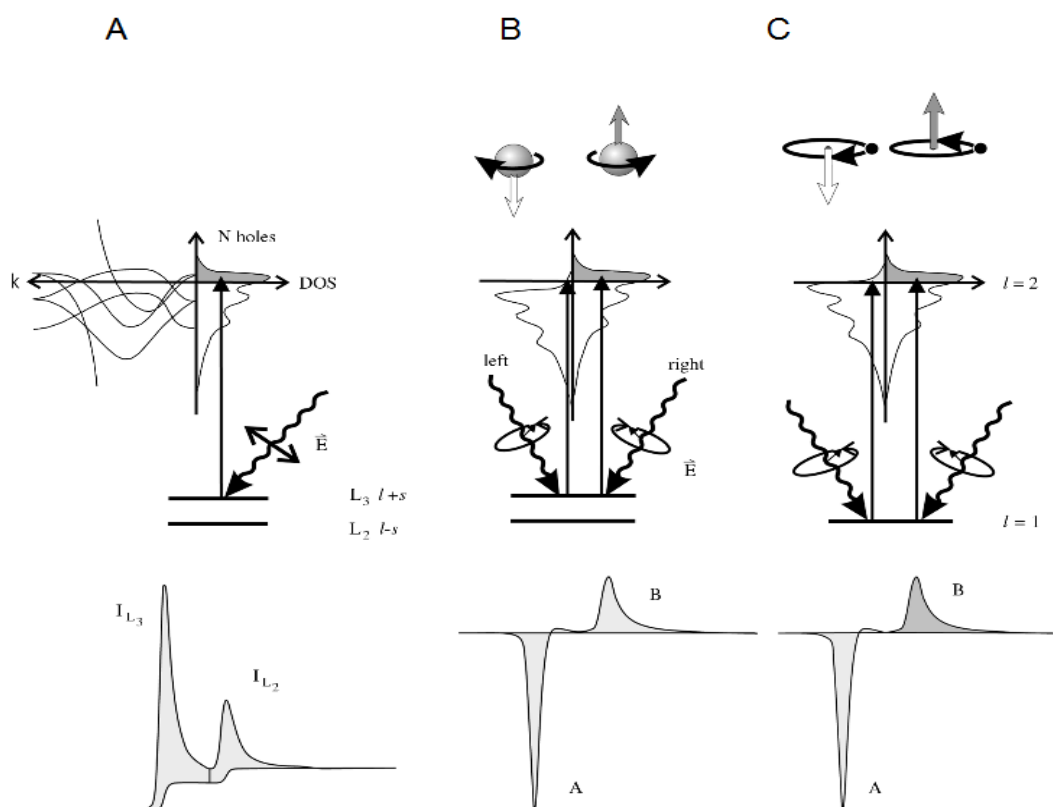


Figure 10. (A) d-Orbital occupation; electronic transitions in conventional L -edge X-ray absorption (B) and (C) X-ray magnetic circular dichroism, illustrated in a one-electron model. By use of circularly polarized X-rays the (B) spin magnetic moment and (C) orbital moment can be determined from the dichroic difference intensities A and B [29].

At the $L_{2,3}$ edges, one can quantitatively measure magnetic properties in terms of spin magnetic moments and orbital moments by using sum rules. For the spin magnetic moment, the sum rule is $A - 2B$, where A is the dichroic intensity at the L_3 edge and B is the dichroic intensity at the L_2 edge. For the orbital moment, the sum rule is $A + B$. One can also study the effect of hybridization of mixed magnetic systems (mostly with oxygen) based on the multiplet analysis of the $L_{2,3}$ edges.

For this experiment, the sample was prepared with DCA² evaporator in the MESA+ cleanroom, by depositing 5 Å thick Co on HOPG and subsequently depositing 2 nm thick Al as capping layer to prevent oxidation. The XAS and XMCD measurements, both at the Co $L_{2,3}$ edge, were performed at beamline I1011 of MAX-laboratory in Lund, Sweden, which uses a circularly polarized undulator to provide left and right circular polarization. The spectra were measured at 77 K by sweeping a 250 Oe magnetic field.

3.3. Vibrating Sample Magnetometer (VSM)

The first VSM was designed by Foner in 1956 and has become generic to all subsequent designs [31]. The VSM works based on Faraday's law of induction which states that a changing magnetic field will produce an electric field. So for the measurement, the magnetized sample is moved periodically at a small fixed amplitude with respect to stationary pick-up coils. The periodic field changes $\partial B(t)$ due to sample movement at a point r inside the detection coils induces a voltage and is given by

$$V(t) = \sum_n \int_A \frac{\partial B(t)}{\partial t} \cdot dA, \quad (10)$$

where A is the area of the coil in a single turn, and the summing is done over n turns of the coils. Hence, for stationary pick-up coils and a uniform and stable external magnetic field, the voltage changes is directly proportional to the magnetic moment of the sample.

For this project, we used a four coils measurement vector VSM (see Fig. 11). Three samples were prepared with the DCA having different thicknesses of Co (0.2 nm, 0.6 nm, and 1.8 nm), then followed by 5 nm thick Al capping layer. Note that we did not intentionally compare these samples with sample for XMCD measurement. The Al capping layer for XMCD measurement was thinner than for VSM measurement. That because the escape length of photoexcited electrons being detected by XMCD is only a few nm. The measurement was conducted at room temperature. After the measurement finished, the samples were peeled off the HOPG substrates with Scotch tape, so only bare HOPG remained to extract the background signal.

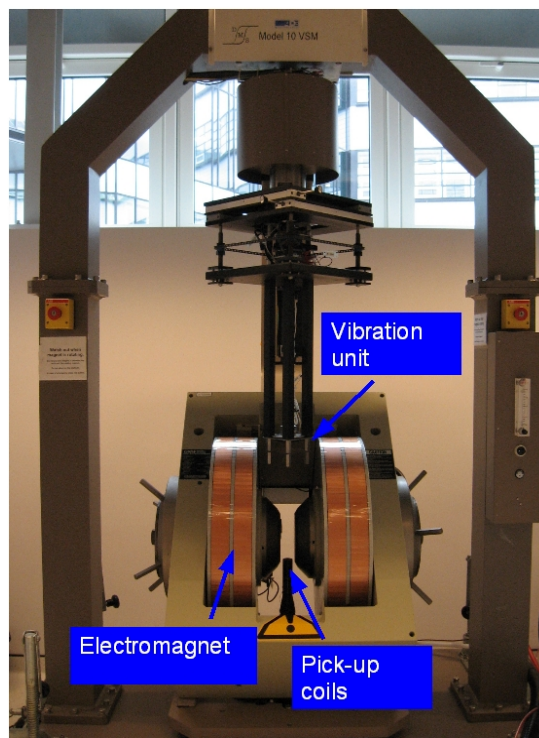


Figure 11. Experimental setup four coils VSM.

² The thicknesses numbers of the samples prepared by DCA were assumed as a thicknesses of a Co continuous film. The experimental results in the next chapter, however, proved the Co were still in the form of clusters indicated by its paramagnetic behavior. A crosscheck with the STM for actual clusters cannot be done due to the infrastructure movement at that time.

4. Results and Discussions

4.1. The Inverse Decay Length Measurement

Before we analyze the results, we reviewed the atomic arrangement of HOPG. In the STM which scans DOS near Fermi level, the HOPG atomic structure was revealed as a triangular structure instead of a honeycombs lattices. This can be explained if one observes the stacking of the atomic layers of HOPG (see Fig. 12). If one sees from the top, HOPG consists of two types of sites; α -sites that have a C atom in the layer below, and β -sites that have no C atoms in the plane below. Due to interaction with below C atom, the states on the α -sites are decoupled from those on the β -sites. β -sites gives higher tunneling current than α -sites because of this different DOS effect. That is the reason why one only observes triangular structures instead of honeycombs with the STM [32].

If we consider the bonding of the C atoms in graphite, graphite's sp^2 hybridization yield strong σ covalent bond with the neighboring C atoms and strengthen the honeycomb structure within the plane. The free electron in the C atoms causes conductivity (enable tunnel from one site to the other within the plane of the layers), and provides weak coupling between α -sites of adjacent layers.

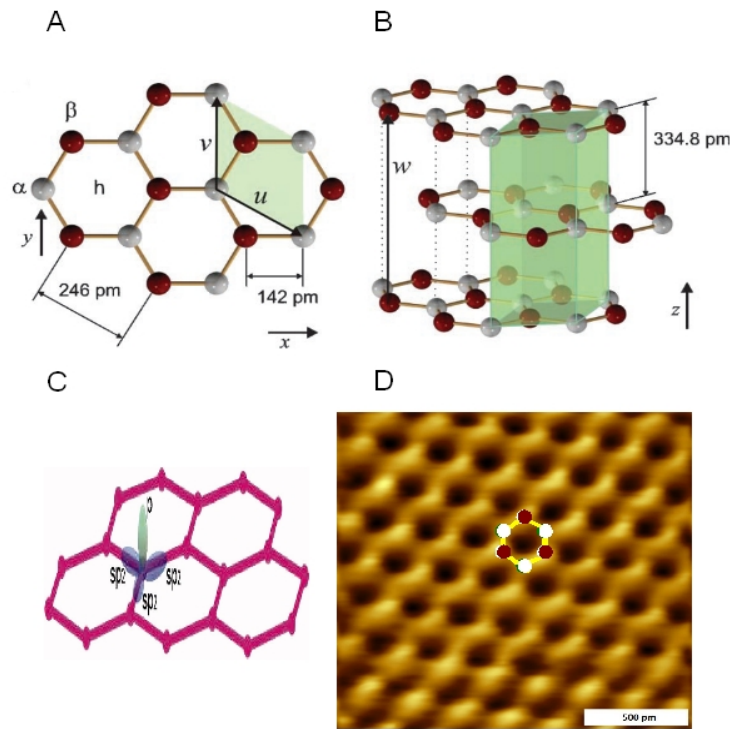


Figure 12. Crystal structure of graphite. The unit cell is shaded in green. (A) Top view on the HOPG surface layer. (B) Perspective view, showing the layered structure [33]. (C) Hybridization in graphene molecule [34]. (D) Atomic resolution of HOPG obtained from our STM measurement taken at $I = 1$ nA, $V = -250$ mV.

STM is the technique that make use of the rapidly decaying electrons wave functions to probe the surface. These decaying waves functions are not physical waves. They have imaginary wave vector k , and they cannot propagate through space like a real wave. For simplicity, if we consider elastic tunneling process, according to the Simmons model (Eq. 8), the decaying factor of imaginary wave vector k is represented on the inverse decay length κ . These decaying wave functions κ provides information on the spatial origin of the tunneling electrons that depends on the electronic state of the sample.

The κ is consists of perpendicular wave vector (k_{\perp}) and parallel wave vector k_{\parallel} (k_x and k_y). In an ideal tunneling processes, the system is translationally invariant along the lateral direction. That means it requires the k_{\parallel} to be conserved and to be a good quantum number. Since the perpendicular wave vector k_{\perp} is not constant, the transmitted tunneling conductance will be dominated by the smallest k_{\parallel} (see Fig. 13).

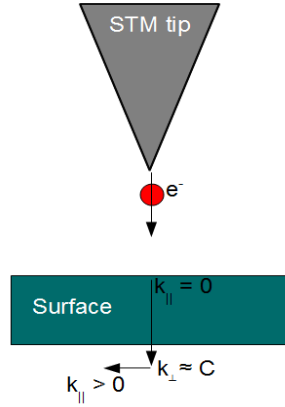


Figure 13. Simplistic illustration of tunneling with STM tip. An electron (illustrated as both particle and wave) tunnel through vacuum barrier transmitted as a wave to the sample surface. The parallel wave vector k_{\parallel} increased from $k_{\parallel} = 0$ to $k_{\parallel} > 0$ after propagate on the surface. The transmitted conductance (tunneling current) therefore is determined mainly by the k_{\parallel} .

However, one should notice where disorder is present in the surface, k_{\parallel} is not conserved anymore. In real cases, disorder is always present and one way to quantify the degree of disorder is to map the inverse decay length κ with I - z spectroscopy STM/STS. In the STM/STS, the inverse decay length can be written as below formula [35]

$$\kappa(V) = \sqrt{k_{\perp}^2 + k_{\parallel}^2} \quad , \quad (11)$$

$$\kappa(V) = \sqrt{\frac{2m}{\hbar^2} \left(\frac{\Phi_t + \Phi_s}{2} - E + \frac{e|V|}{2} \right) + k_{\parallel}^2} \quad , \quad (12)$$

where $\Phi_{t,s}$ is the work function of the tip and sample, respectively; and E is the energy relative to the Fermi level. Electronic states with small k_{\parallel} have the smallest κ and thus contribute most to the tunneling current. For graphite, the limit (upper bound value) of the k_{\parallel} is elastic tunneling at the K points of the Brillouin zone, hence the k_{\parallel} must be large ($k_{\parallel} = K = 4\pi/(3d_{Bo}) = 4\pi/(3 \times 2.46 \text{ \AA}) = 1.7 \text{ \AA}^{-1}$ [36]). So by filling in all the known numbers in Eq. 12, we can determine the upper bound spatial mapping of the inverse decay length (See Appendix A).

To determine how much it deviates from the upper bound value, we have done I - z spectroscopy with a Nanosurf portable STM, which works under atmospheric conditions. We used this STM for the sake of simplicity for taking measurement. The spectrum were taken only when we achieved atomic resolution and only with one tip to reduce tip inhomogeneity effects. From the Simmons model on Eq. 5, $I(V,z) \propto e^{-2\kappa z}$. By plotting $\ln(I)$ versus z , the slope gives -2κ .

In Fig. 14, we plotted the upper bound and experimental κ versus V (for data source see Appendix A). It is shown that in the experiment result, the κ is much lower than the upper bound 1.7 \AA^{-1} due to smaller k_{\parallel} . From this result one can justify that electrons from the STM tip cannot directly tunnel to the K points mainly because the STM tip has only one state for tunnelling centered at $k_{\parallel} = 0$, which makes the tunneling electrons have a low transmission probability. In order to tunnel to the K points, electrons need to be assisted by phonons.

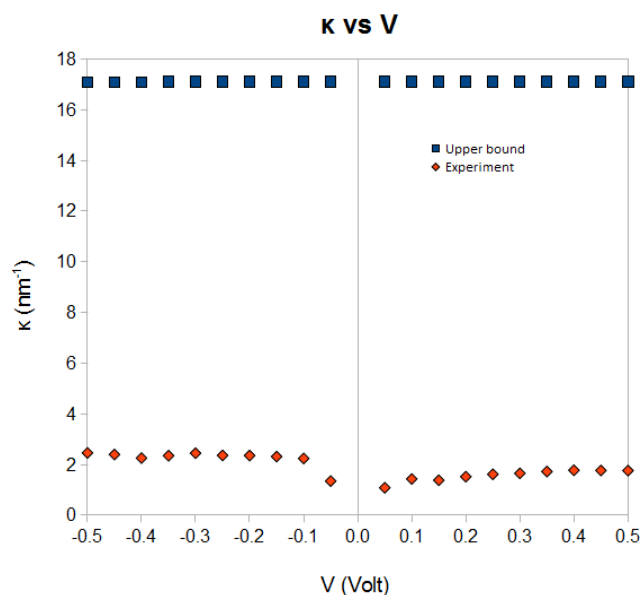


Figure 14. The plot of upper bound and experimental κ versus V .

4.2. STM/STS Cobalt Nanoclusters on HOPG

4.2.1. Morphology Study

Various systems consisting of Co nanoclusters on a substrate has been reported due to their distinctive electronic and magnetic properties. In the nanoscale regime, these physical properties depends on the Co clusters size, and their interaction with the substrate. At sufficiently small size, their electronic states becomes discrete and interesting physical phenomena can be observed, such as, the Kondo effect [37-39], and increased of the magnetic moment per atom [40-42].

Before we analyze the results, we should pay attention on the Co atomic structure. In this experiment, we assumed that the Co crystal structure will be hcp. From References [2-3, 43], hcp Co has cell parameters (see Fig. 15): $a, b = 2.42 - 2.5071 \text{ \AA}$; $c = 4.0695 - 4.08 \text{ \AA}$; $\alpha, \beta = 90^\circ$; and $\gamma = 120^\circ$. That means that one ML of Co will equal $c/2 = 2.0348 - 2.04 \text{ \AA}$ in height.

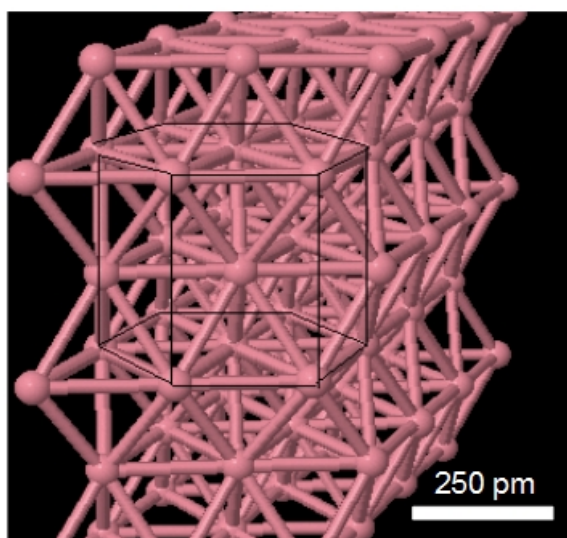
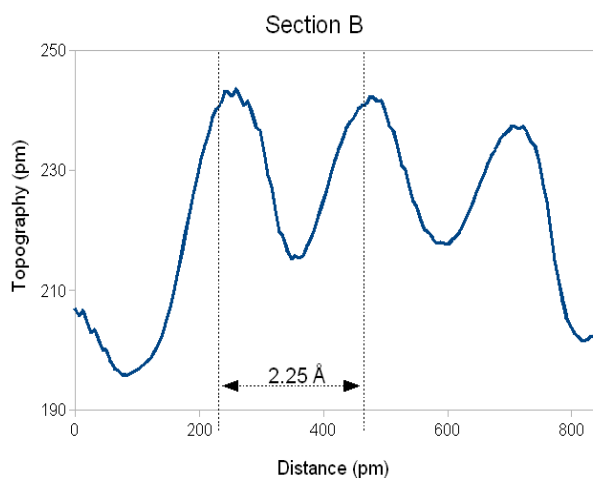
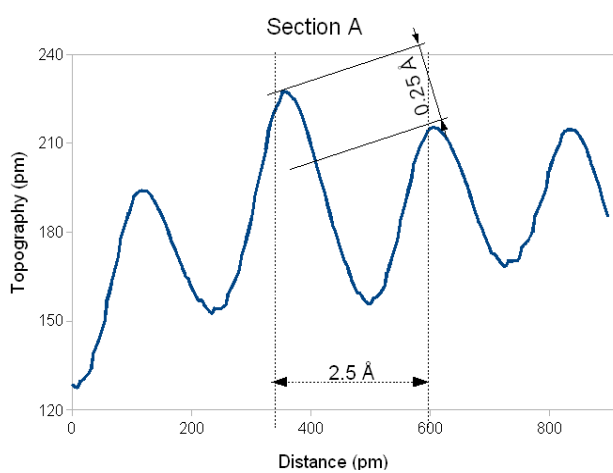
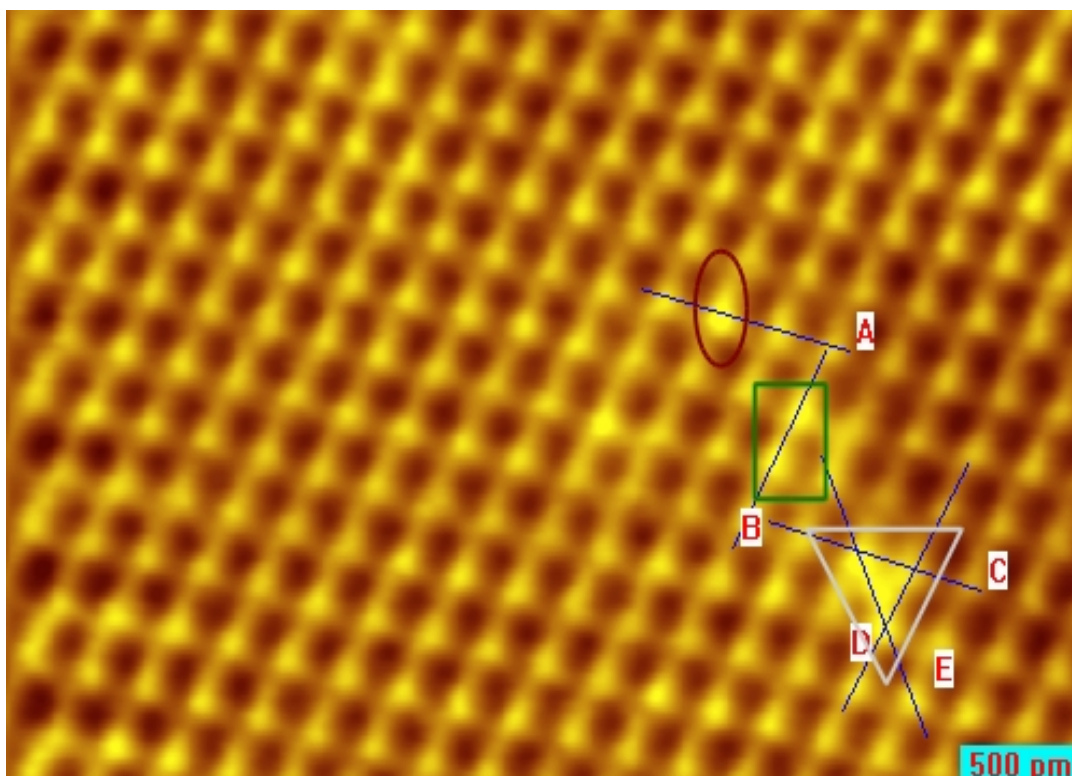


Figure 15. Hcp Co crystal structure [43].

In this STM study we are aiming to explore the growth of the Co nanoclusters on HOPG. There are two predictions about favorable sites where Co adatoms would preferably reside [44-46]. Firstly, it was assumed Co adatoms would sit in the middle of honeycomb graphite lattice [45-46]. This prediction was not correct based on our STM image in Fig. 16. It appears that the Co adatoms were firstly grown on β -sites of the HOPG, just like other metal adatoms (Cu, Ag, Au, and Al) .



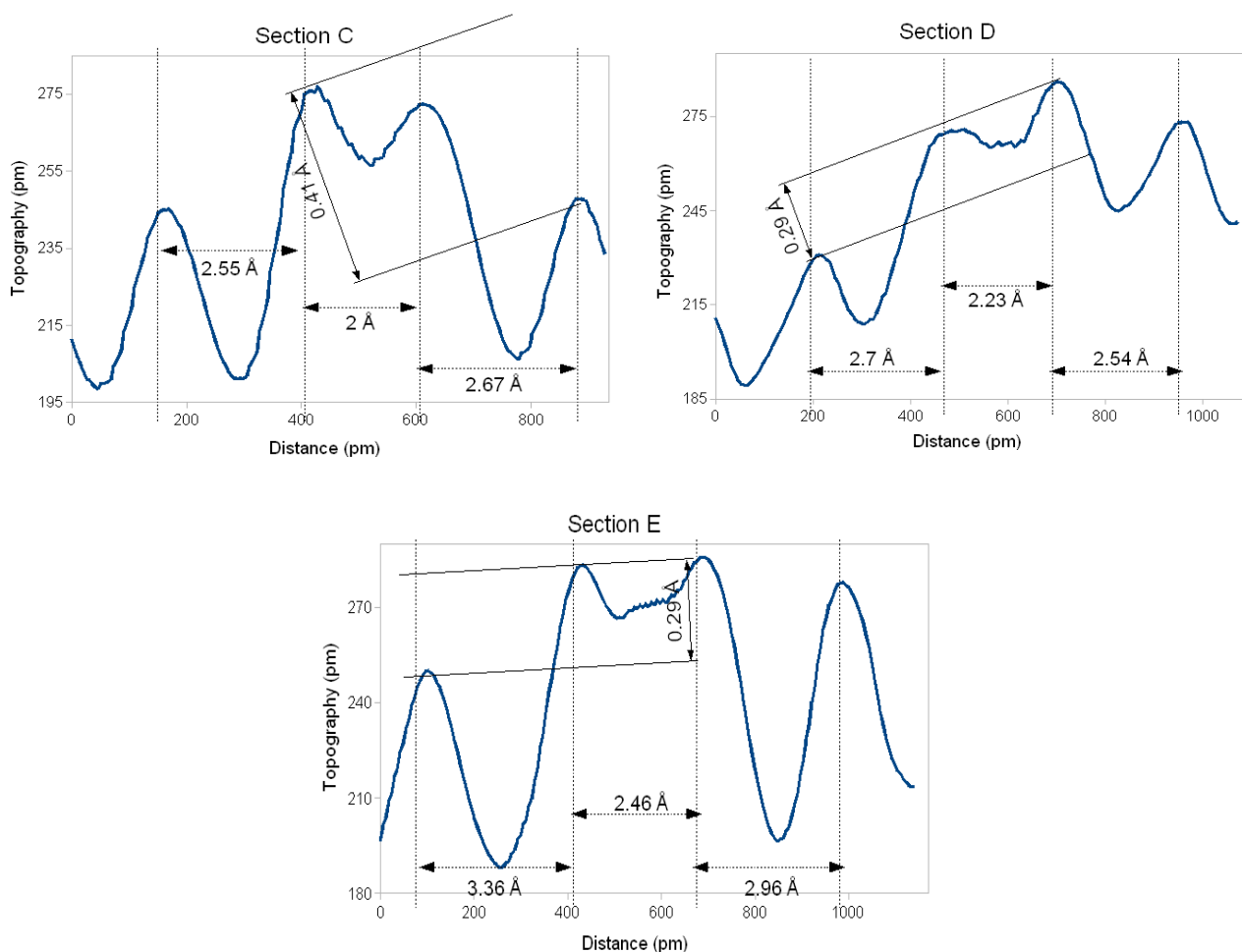


Figure 16. STM topography Image of Co nanoclusters taken at $I = 1.04$ nA, $V = -219$ mV. Deposition time was 2 min 32 sec. Co adatoms sits epitaxially on the β -sites of HOPG. Red circle = one Co adatoms sits on the β -sites(see Section A). Green box = Two Co adatoms sit on the β -sites. These adatoms do not make any bonding between themselves (see Section B). Gray triangle = Co adatoms made a bonding on the β -sites and expanded but let the over-hole site unoccupied; the bonding of the network is confirmed in Sections C-E.

Based on STM image (see Fig. 16), the β -sites of the HOPG were the most stable sites for Co adatoms and the over-hole sites were the least favorable sites. This was related to the bonding and hybridization in graphite. The C-atoms at the β -sites were not bonded to an atom in the layer below, therefore their orbitals were free to hybridize with the Co adatoms. Subsequently, the Co adatoms were filling other sites except the over-hole sites. Although we cannot resolve the STM image further, it was more probable that Co adatoms filled the α -sites sites before the over-bond sites. That because, the α -sites were not only used their free electrons for facilitate coupling with below C-atoms layer, but also were used some of them for facilitate hybridization with Co adatoms. The over-hole sites were hindered by Co adatoms because when Co adatoms adsorbed and moved (to find the most stable configuration), they only moved along the bond, and the over-hole sites were in fact a deep valley.

As for comparison, we reviewed one article about DFT computer calculations of Ag metal adatoms systems on HOPG [44]. Based on their results, it was concluded that adsorption of our Co adatoms is similar to the Ag adatoms system. The adsorption of metal adatoms on HOPG starts with following order: β -sites (which have the strongest binding energy), α -sites, over-bond sites, and the last is over-hole sites (see Table 3).

Site	E_b (eV)	h (Å)
α	0.423	2.570
β	0.425	2.568
Over-bond	0.420	2.571
Over-hole	0.391	2.614

Table 3. Calculated values of the binding energy E_b and the height of silver atoms on the HOPG [44].

If we observe the sectioning of each marked colored region on Fig. 16, we can check whether the Co adatoms are making a bond between themselves or not, by probing the electron density in between the atoms. We can analyze the sequence of the peaks and the valleys by XPMPro software sectioning. We assumed that if one peak followed by one valley sequentially, that means no bonding between two adatoms. But, if between two adatoms, there are two peaks recombined and there is no valley in between, it means those two adatoms were bonded. This qualitative method is valid for argument since we cannot determine precisely the bond height between two adatoms due to STM tip convolution. For example in Section A, we can see that peaks were always followed by valleys, which is an indication that the adatom is only one, and free from bonding with other adatoms. In Section B, two adatoms that sit close to each other also showed peak and valley between them, confirming that instead of a dimer, they are just two adatoms sitting close to each other without bonding. However, if we check the gray triangular region, all sections that crossed adatoms (Sections C-E) showed that there are bonding between all those Co adatoms.

The sectioning analysis in Fig. 16 also showed that Co adatoms at sub-monolayer (ML) thickness grow epitaxially on HOPG. This is proved by the fact that in all Sections (A-E) the distance between two adjacent Co adatoms was close to 2.46 Å, which is the separation of two β atoms in HOPG. The apparent height (less than 0.5 Å) is much smaller than real Co atoms because of the hybridization and physisorption between Co and HOPG sites. The aspect ratio of the adatoms (h/d) for all the Sections (A, C-E) was constant ≈ 0.1 -0.2.

However, the epitaxial growth is a local effect. The growth is not always homogeneous on the HOPG surface (see Fig. 17) regardless it comes from the same batch of sample. By doing section analysis (Sections A to F), it showed that this Co adatoms has average diameter and height of 4.28 Å and 3.07 Å respectively. The diameter and height of this cluster is almost double than the adatoms in Fig. 16 and for the height it is about ten times bigger. This made the adatoms appearing as a nanocluster with thickness around 1.5 ML (1 ML Co height is 2.04 Å) and aspect ratio (h/d) around 0.71. We believe that this apparent nanocluster was a growth defect, since it was not due to a tip artefact (proved by maintained periodicity of 2.46 Å of β -sites HOPG). The growth defect possibly can be caused by the unwanted molecule (i.e. water molecule) on the HOPG. So when the adatoms move to find favorable nucleation site, this impurity molecule stop the movement and stabilize the Co adatoms.

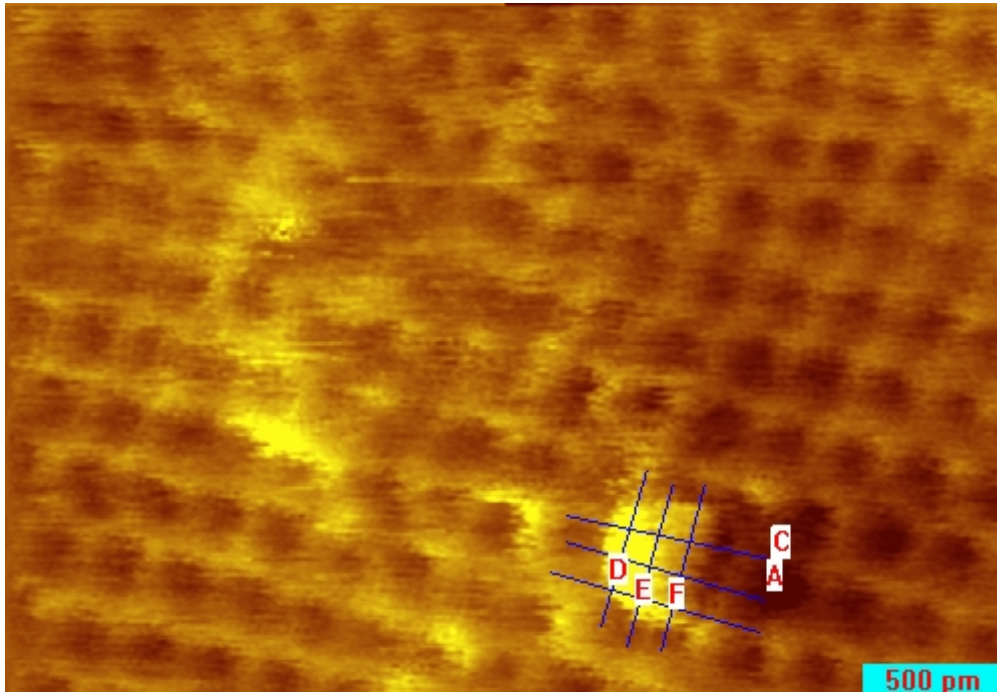


Figure 17. The STM Image of a Co nanocluster with deposition time was 2 min 32 sec taken at $I = 1.05$ nA, $V = -218$ mV. We believed that this nanocluster was a growth defect. The diameter and height of these cluster showed in the Table 4.

Section	Diameter (in Å)	Height (in Å)
A	3,62	2,74
B	4,01	4,01
C	4,09	2,42
D	3,93	3,1
E	5,16	3,53
F	4,89	2,59
Average	4,28	3,07

Table 4. The diameter and height of each from Section A to F on Fig. 17. The measurements were done with XPMPro software.

We also analyzed the distribution of Co nanoclusters. The Co coverages in our study were below 5% for which the Co growth was found to follow the Volmer-Weber mode, independent of deposition time. And to study the coverage, we remained in the nucleation-dominated regime, thus allowing us to image the isolated adatoms and nanoclusters (from Table 5, average mean size of diameter and height are 3.36 nm and 0.49 nm respectively) of Co. The aspect ratio of the nanoclusters (h/d) is ≈ 0.15 .

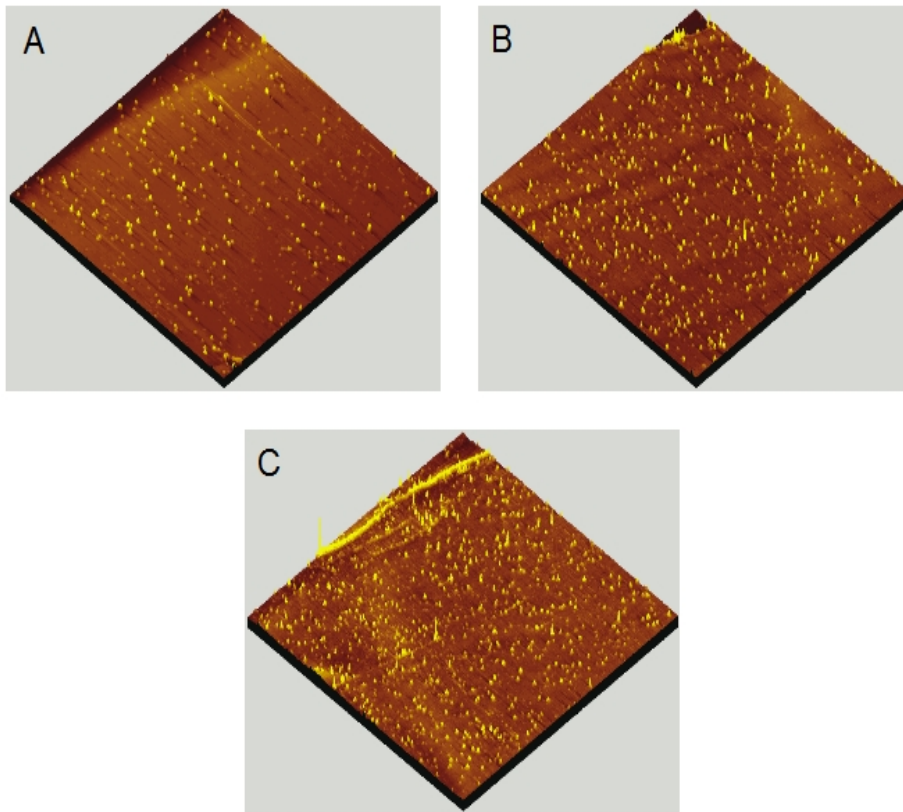


Figure 18. The 3 nm x 3 nm STM Image of Co nanoclusters of increment deposition time (A) 1 min 32 sec, (B) 2 min 32 sec, and (C) 5 min. Deposition were done in STM evaporation chamber at room temperature.

Coverage	Diameter (in nm)		Height (in nm)	
	Mean Size	Std Dev	Mean Size	Std Dev
A	3,40	0,15	0,42	0,06
B	3,33	0,23	0,50	0,03
C	3,36	0,23	0,56	0,05

Table 5. The diameter and height of coverage a, b, and c from Fig. 18. The statistical analysis were done with XPMPro software by counting five hundreds nanoclusters from each coverage.

We also found that even though some regions on the HOPG had more intense deposition of Co compare to another, the "true" nanoclusters always kept the aspect ratio (h/d) constant $\approx 0.1-0.2$. In Fig. 19, this nanoclusters were agglomerated into larger size than the mean value diameter and height; 3.4 ± 0.2 nm and 0.49 ± 0.045 nm, respectively; and made dome-like appearance even at lower deposition time (1min 45 sec), with maintained typical aspect ratio (h/d) = 1.52 nm/ 9.41 nm ≈ 0.16 .

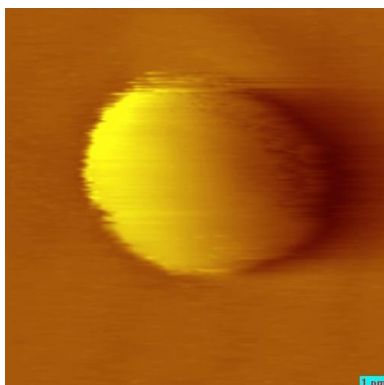


Figure 19. STM image of an individual size-selected Co nanoparticles with diameter and height 9.41 nm and 1.52 nm, respectively. The Co deposition time was 1 min 45 sec at room temperature. The image was taken with W tip at $I = 0.15$ nA and $V = -495$ mV.

4.2.2. Electronic Properties Study

The electronic properties of Co nanoclusters on HOPG were studied by I-V STS. We used grid spectroscopy which allows us to measure I-V at certain pixel while scanning, hence minimizing the drift effect. For grid I-V spectroscopy, the measurement was done with an electrochemically etched tungsten (W) tip. This electrochemically etched W tip is generally sharper and more durable than a manually cut PtIr tip. However, it is not possible to distinguish the Co nanoclusters from the HOPG substrate mainly due to their similar conductivity behavior. As been mentioned before, the conductivity of graphite comes from the free electron on the orbital $2p_z$ which forms π -bond for high in-plane conductivity.

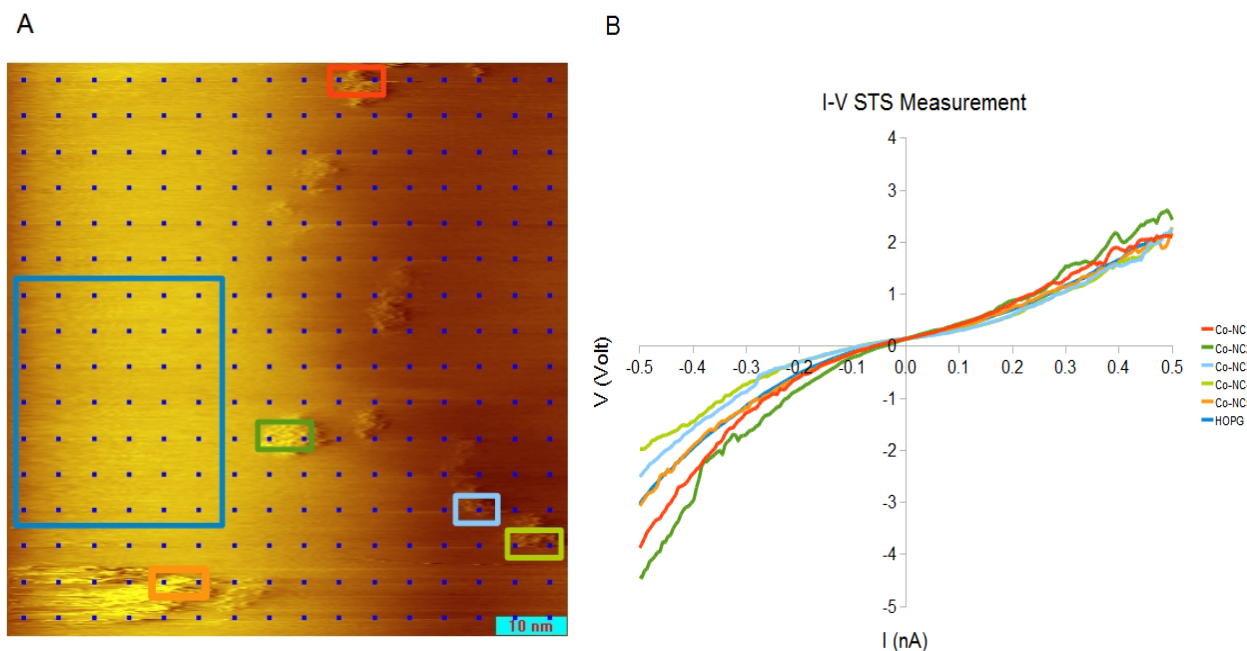


Figure 20. (A) STM image of Co nanoclusters on HOPG. The Co deposition time was 1 min 45 sec at room temperature. (B) The image and I-V spectroscopic data were taken at $I = 1$ nA and $V = 322$ mV at 95 K. The I-V was taken with grid spectroscopy 16×16 resulting in 256 I-V curves. The I-V curves of HOPG were taken from average I-V in the biggest box (contains 42 spectra). For Co nanoclusters, the I-V curves were averaged from each colored region.

4.3. XMCD Cobalt Nanoclusters

Ferromagnetism in $3d$ TM is collective effect that depends on the overlap of electron clouds on the neighboring atoms, and thus distance between them. In our sample, we had randomly distributed Co nanoclusters which made the neighboring effect and necessary exchange interaction for ferromagnetism behavior was suppressed. Also since the dimension of the Co nanoclusters was very small, magnetic ordering tends to decrease as fluctuation (especially because of thermal disturbances) become more important. Once magnetized, the thermal stability of magnetic nanoclusters (or nanoparticles) is defined as

$$\tau = \tau_0 \exp\left(\frac{K_U V}{k_B T}\right), \quad (13)$$

where τ is the magnetic reversal time, τ_0 is constant ($\sim 10^{-10}$ s), K_U is the anisotropy energy, V is the particle volume, and $k_B T$ is the thermal energy. A decrease in the clusters size will greatly increase the magnetic reversal time.

Based on that information, we expect our Co nanoclusters to behave as paramagnetic material because of its size and random distribution (less interaction with neighboring clusters). The XMCD result showed very weak dichroism effect at 250 Oe and 77 K. Since, the magnetic moment was too small, we cannot extract the magnetic properties m_s and m_o for Co nanoclusters with the sum rule. The reasons can be due to these possibilities: the Co nanoclusters were intermixed with impurities at the interface, or the magnetic field was not strong enough to magnetize the Co nanoclusters. However, the first possibility was not happened. The lack of multiplet structure in X Ray Absorption spectra $L_{2,3}$ edges showed that the Co nanoclusters was not oxidized or hybridized with unexpected impurities. Therefore we did VSM measurements to extract the magnetic moment of Co nanoclusters which will be presented in the next section.

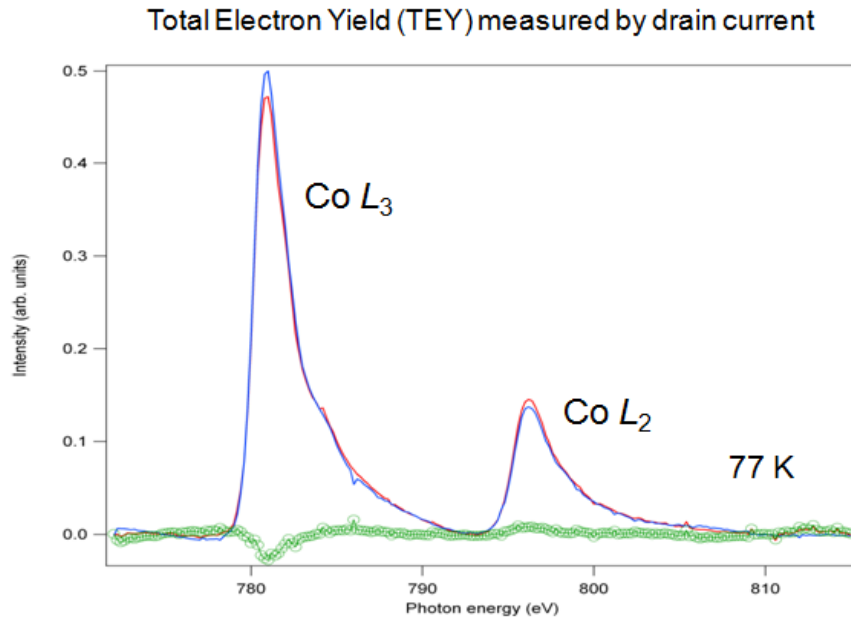


Figure 21. Co X-Ray absorption spectra for parallel μ_+ (red line) and antiparallel μ_- (blue line) direction of light polarization and field-induced magnetization. The dichroism signal is obtained by subtraction of the absorption spectra and normalized (green lines). An arctan background shape was subtracted from the data.

4.4. VSM

VSM measurement confirmed the paramagnetic behavior of Co nanoclusters. It showed that higher magnetization corresponds to the increasing amount of Co deposited. From the typical paramagnetic S curve, it can be concluded that even the Co clusters in the nominally 1.8 nm thick film were still paramagnet with magnetization saturation M_s around 40×10^{-9} emu.

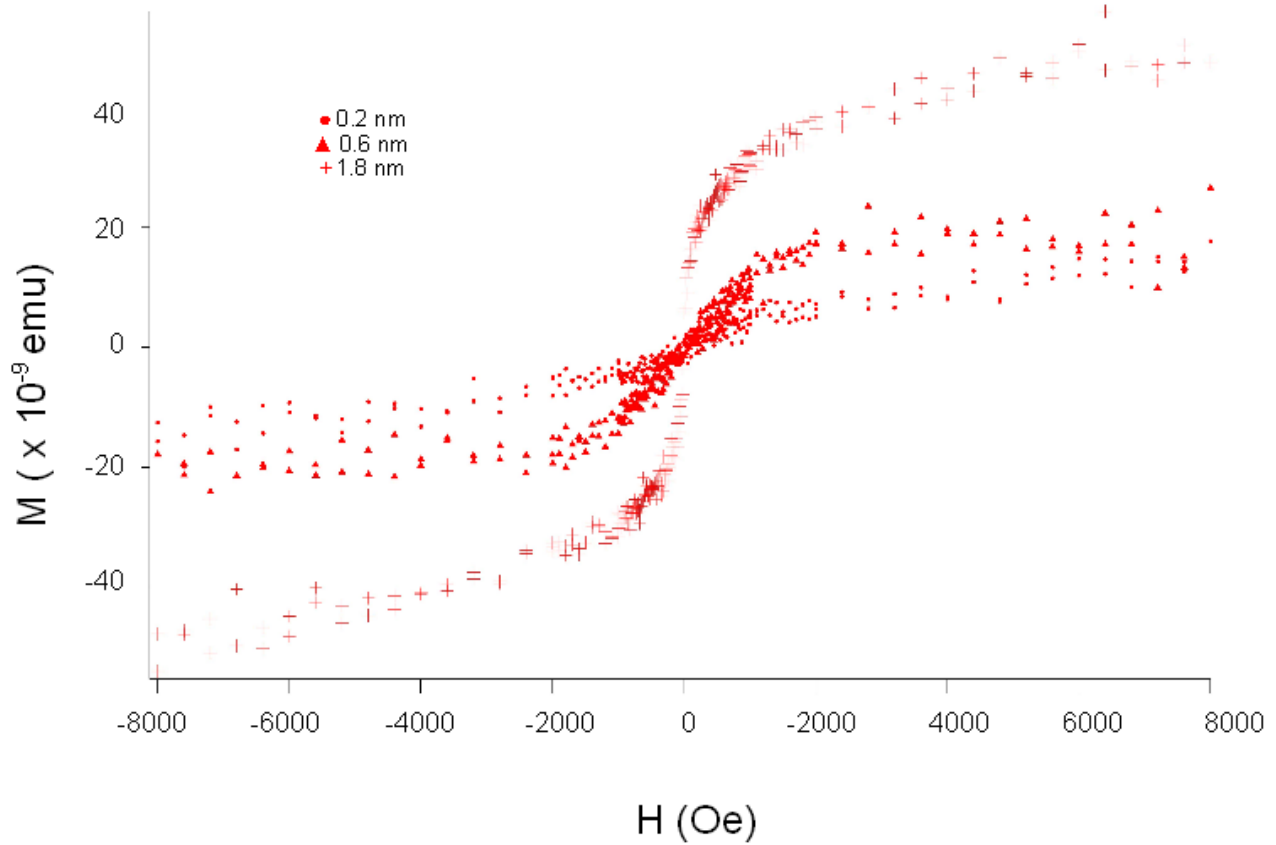


Figure 22. VSM measurement at room temperature from three different variant of Co thickness. The measurement has been subtracted with the bare HOPG signal.

5. Conclusions and Recommendations

5.1. Conclusions

From these investigations we can draw several conclusions. Firstly, we characterized the electronic properties of HOPG by means of I - z spectroscopy which represents electronic tunneling properties of the tip-graphite system at low bias range (near Fermi level). It was shown that, the tip-graphite system is hardly able to tunnel from and to the K points due to low wave vector $k_{||}$ value (maximum experimental value $k_{||}$ is 2.46 nm^{-1} at -0.5 V).

We observed individual Co ad-atoms initially sitting at the β -sites of the graphite surface lattice, and subsequently filling the other sites to form nanoclusters. The Co nanoclusters growth was found to follow the Volmer-Weber mode, and always kept the aspect ratio (h/d) constant ≈ 0.1 - 0.2 . The mean diameter and height of the isolated nanoclusters are $3.4 \pm 0.2 \text{ nm}$ and $0.49 \pm 0.045 \text{ nm}$ respectively.

The nanoclusters behave as paramagnetic indicated by XMCD and VSM measurement. Even though the magnetic moment can not be extracted with the XMCD, the measured spectra revealed that the adsorbed Co clusters on HOPG were metallic, as evidenced by the lack of multiplet structure at the Co $L_{2,3}$ edges. Other magnetic properties characterization was done using VSM revealed the paramagnetic spectrum for different thicknesses of Co. The value of M_s measured was around $40 \times 10^{-9} \text{ emu}$ for Co clusters in the nominally 1.8 nm thick film.

5.2. Recommendations

For the next experiments we recommend the following:

Firstly we need to make another batch sample from the DCA with the same deposition parameters (except without Al capping layer) to be crosschecked with the STM. This can correlate the result of XMCD and VSM with the nanoclusters size.

Secondly, we are going to build the heater inside the deposition chamber of the STM. This is expected to help formation of epitaxial structure on HOPG. It is known that surface diffusion (D) is a thermally activated process. With constant deposition rate (F) and given surface diffusion (D), the ratio D/F determines how far the average distance between two adatoms to meet each other. If the ratio D/F is large, then growth process happens close to equilibrium condition and determined by thermodynamics, hence the adatoms or nanoclusters have enough time to reach minimum energy configuration and arrange themselves orderly. If the ratio D/F is small, then the deposition mainly determines by kinetics which is less-ordered growth process [47].

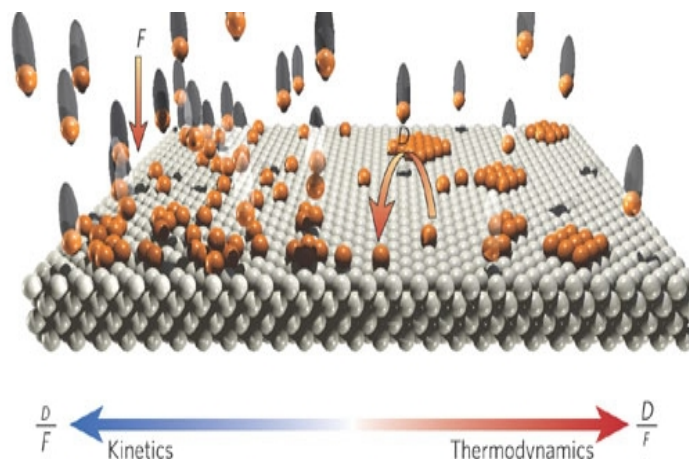


Figure 23. Schematic illustration of atoms or molecules deposited from the vapor phase [47].

Finally, we will also try to deposit CoFeB in the next experiment. The CoFeB is amorphous during deposition and can be crystallized with post-annealing process. CoFeB is also convenient to be used rather than pure ferromagnetic metals since it is not easily oxidized at the interface and higher polarization and TMR can be achieved [48].

6. Acknowledgments

I would like to say my deepest gratitude to all of my supervisors. For Wilfred van der Wiel and Michel de Jong who supervise and host me in my master project. Thank you very much for your best guidance. For Harold Zandvliet who is always be there whenever a student needs his help. Also for Johnny Wong with his critical think, hard work ethics, and his willingness to stay with the STM whatever it takes for sure has taught me a lot.

Thanks to Martin Siekman for his help when STM had some technical problem; Avijit Kumar for his help teasing up STM tip with his magic finger. Avijit and with Amirmehdi Saedi also have been so helpful for answering my questions about STM. From NE, Yunjae Lee and Sandeep for answering questions about spintronics; Tian Gang for any instruments he taught me; and also for Maarten Groen for proofreading my thesis.

Working partly in two groups for sure made me met people along the way. Thanks to Harold and Bene Poelsema for providing me a place in the group when I were project-less. I feel gratitude for all member of SSP group, and all member of NE for their companions during my last year as a student. Special thanks to Maciej (and with Avijit) for his invitation to Poland and his warm-hearted family who refreshed me from this project. Guy's let's celebrate life even more.

Tante Sani & Oom Henk, and Oma Yet & fam, for being my family in the Netherlands. And for Tante Ineke, thank you for your kindness, you are the best thing I have in the Netherlands.

Finally, my greatest thanks is for my friends and families in Indonesia. Thank you so much for your unconditional love and support.

7. References

1. W. J. M. Naber, S. Faez, W.G. van der Wiel, *Organic spintronics* J. Phys. D: Appl. Phys., 2007. **40**(12): p. R205–R228.
2. V. M. Karpan, G. Giovannetti, P. A. Khomyakov, M. Talanana, A. A. Starikov, M. Zwierzycki, J. van den Brink, G. Brocks, and P. J. Kelly, *Graphite and Graphene as Perfect Spin Filters*. Phys. Rev. Lett., 2007. **99**(176602): p. 1-4.
3. V. M. Karpan, P. A. Khomyakov, A. A. Starikov, G. Giovannetti, M. Zwierzycki, M. Talanana, G. Brocks, J. van den Brink, and P. J. Kelly, *Theoretical prediction of perfect spin filtering at interfaces between close-packed surfaces of Ni or Co and graphite or graphene*. Phys. Rev. B, 2008. **78**(195419): p. 1-11.
4. Andreas Moser, Kentaro Takano, David T Margulies, Manfred Albrecht, Yoshiaki Sonobe, Yoshihiro Ikeda, Shouheng Sun, and Eric E Fullerton, *Magnetic recording: advancing into the future* J. Phys. D: Appl. Phys. , 2002. **35**(19): p. R157-R167.
5. M. N. Baibich, J. M. Broto, A. Fert, F. Nguyen Van Dau, F. Petroff, P. Etienne, G. Creuzet, A. Friederich, and J. Chazelas, *Giant Magnetoresistance of (001)Fe/(001)Cr Magnetic Superlattices*. Phys. Rev. Lett., 1988. **61**(21): p. 2472–2475.
6. G. Binasch, P. Grüneberg, F. Saurenbach, and W. Zinn, *Enhanced magnetoresistance in layered magnetic structures with antiferromagnetic interlayer exchange*. Phys. Rev. B, 1989. **39**(7): p. 4828–4830
7. Claude Chappert, Albert Fert, and Frédéric Nguyen Van Dau, *The emergence of spin electronics in data storage*. Nat. Mat, 2007. **6**: p. 813-823.
8. Igor Žutić, Jaroslav Fabian, and S. Das Sarma, *Spintronics: Fundamentals and applications*. Rev. Mod. Phys. , 2004. **76**(2): p. 323-410.
9. Christian Heiliger, Peter Zahn, and Ingrid Mertig, *Microscopic origin of magnetoresistance*. Materials Today, 2006. **9**(11): p. 46-54.
10. Jullière, M., *Tunneling between ferromagnetic films* Phys. Lett. A, 1975. **54**(3): p. 225-226.
11. T. Miyazaki, and N. Tezuka, *Giant magnetic tunneling effect in Fe/Al₂O₃/Fe junction*. J. Magn. Magn. Mater., 1995. **139**(3): p. L231-L234.
12. J. S. Moodera, Lisa R. Kinder, Terrilyn M. Wong, and R. Meservey, *Large Magnetoresistance at Room Temperature in Ferromagnetic Thin Film Tunnel Junctions*. Phys. Rev. Lett., 1995. **74**(16): p. 3273-3276.
13. J. Mathon, and A. Umerski, *Theory of tunneling magnetoresistance of an epitaxial Fe/MgO/Fe(001) junction*. Phys. Rev. B, 2001. **63**(220403(R)): p. 1-4.
14. W. H. Butler, X.-G. Zhang, T. C. Schulthess, and J. M. MacLaren, *Spin-dependent tunneling conductance of Fe/MgO/Fe sandwiches*. Phys. Rev. B, 2001. **63**(054416): p. 1-12.
15. S. Yuasa, and D. D. Djayaprawira, *Giant tunnel magnetoresistance in magnetic tunnel junctions with a crystalline MgO(001) barrier* J. Phys. D: Appl. Phys., 2007. **40**(21): p. R337-R354.
16. Shinji Yuasa, Taro Nagahama, Akio Fukushima, Yoshishige Suzuki, & Koji Ando, *Giant room-temperature magnetoresistance in single-crystal Fe/MgO/Fe magnetic tunnel junctions*. Nat. Mat, 2004. **3**: p. 868-871.
17. S. Ikeda, J. Hayakawa, Y. Ashizawa, Y. M. Lee, K. Miura, H. Hasegawa, M. Tsunoda, F. Matsukura, and H. Ohno, *Tunnel magnetoresistance of 604% at 300 K by suppression of Ta diffusion in CoFeB/MgO/CoFeB pseudo-spin-valves annealed at high temperature*. Appl. Phys. Lett., 2008. **93**(082508): p. 1-3.
18. P. LeClair, J. K. Ha, H. J. M. Swagten, J. T. Kohlhepp, C. H. van de Vin, and W. J. M. de Jonge, *Large magnetoresistance using hybrid spin filter devices*. Appl. Phys. Lett., 2002. **80**(4): p. 625-627.
19. Michael G. Chapline, and Shan X. Wang, *Spin filter based tunnel junctions*. J. Appl. Phys. , 2006. **100**(123909): p. 1-4.
20. L. Esaki, P. J. Stiles, and S. von Molnar, *Magnetointernal Field Emission in Junctions of Magnetic Insulators*. Phys. Rev. Lett., 1967. **19**(15): p. 852-854.
21. J. S. Moodera, X. Hao, G. A. Gibson, and R. Meservey, *Electron-Spin Polarization in Tunnel Junctions in Zero Applied Field with Ferromagnetic EuS Barriers*. Phys. Rev. Lett., 1988. **61**(5): p. 637-640.
22. X. Hao, J. S. Moodera, and R. Meservey, *Spin-filter effect of ferromagnetic europium sulfide tunnel barriers*. Phys. Rev. B, 1990. **42**(13): p. 8235-8243.
23. Jagadeesh S Moodera, Tiffany S Santos, and Taro Nagahama *The phenomena of spin-filter tunnelling*. J. Phys.: Condens. Matter 2007. **19**(165202): p. 1-24.
24. J. S. Moodera, R. Meservey, and X. Hao, *Variation of the electron-spin polarization in EuSe tunnel junctions from zero to near 100% in a magnetic field*. Phys. Rev. Lett., 1993. **70**(6): p. 853-856.

25. Tiffany S. Santos, and Jagadeesh S. Moodera, *Observation of spin filtering with a ferromagnetic EuO tunnel barrier*. Phys. Rev. B, 2004. **69**(241203(R)): p. 1-4.
26. A. V. Ramos, M.-J. Guittet, J.-B. Moussy, R. Mattana, C. Deranlot, F. Petroff, and C. Gatel, *Room temperature spin filtering in epitaxial cobalt-ferrite tunnel barriers*. Appl. Phys. Lett., 2007. **91**(122107): p. 1-3.
27. Yuri Nukaga, Mitsuru Ohtake, Fumiyo Kirino and Masaaki Futamoto, *Microstructure of Co(1120) epitaxial thin films, grown on MgO(100) single-crystal substrates* J. Phys.: Conf. Ser., 2010. **200**(072071): p. 1-4.
28. Harold J.W. Zandvliet, and Arie van Houselt, *Scanning Tunneling Spectroscopy*. Annual Review of Analytical Chemistry 2009. **2**(1): p. 37-55.
29. Stöhr, J., *Exploring the microscopic origin of magnetic anisotropies with X-ray magnetic circular dichroism (XMCD) spectroscopy*. J. Magn. Magn. Mater., 1999. **200**(1-3): p. 470-497.
30. Groot, F.d., *High-Resolution X-ray Emission and X-ray Absorption Spectroscopy*. Chem. Rev., 2001. **101**(6): p. 1779-1808.
31. Foner, S., *Versatile and Sensitive Vibrating-Sample Magnetometer*. Rev. Sci. Instrum., 1959. **30**(7): p. 548-557.
32. David Tománek, S.G.L., H. Jonathon Mamin, David W. Abraham, Ruth Ellen Thomson, Eric Ganz, and John Clarke *Theory and observation of highly asymmetric atomic structure in scanning-tunneling-microscopy images of graphite*. Phys. Rev. B, 1987. **35**(14): p. 7790–7793.
33. Stefan Hembacher, Franz J. Giessibl, Jochen Mannhart, and Calvin F. Quate *Revealing the hidden atom in graphite by low-temperature atomic force microscopy*. PNAS, 2003. **100**(22): p. 12539–12542.
34. Pachos, J.K., *Manifestations of topological effects in graphene*. Contemporary Physics, 2009. **50**(2): p. 375-389.
35. R. J. de Vries, A. Saedi, D. Kockmann, A. van Houselt, B. Poelsema, and H. J. W. Zandvliet, *Spatial mapping of the inverse decay length using scanning tunneling microscopy*. Appl. Phys. Lett., 2008. **92**(174101): p. 1-3.
36. L. Vitali, M. A. Schneider, K. Kern, L. Wirtz, and A. Rubio, *Phonon and plasmon excitation in inelastic electron tunneling spectroscopy of graphite*. Phys. Rev. B, 2004. **69**(121414(R)): p. 1-4.
37. V. Madhavan, W. Chen, T. Jamneala, M. F. Crommie, and N. S. Wingreen, *Tunneling into a Single Magnetic Atom: Spectroscopic Evidence of the Kondo Resonance* Science, 1998. **280**(5363): p. 567-569.
38. H. C. Manoharan, C. P. Lutz, and D. M. Eigler, *Quantum mirages formed by coherent projection of electronic structure* Nature, 2000. **403**: p. 512-515
39. Teri W. Odom, Jin-Lin Huang, Chin Li Cheung, and Charles M. Lieber, *Magnetic Clusters on Single-Walled Carbon Nanotubes: The Kondo Effect in a One-Dimensional Host* Science, 2000. **290**(5496): p. 1549-1552.
40. J. P. Bucher, D. C. Douglass, and L. A. Bloomfield, *Magnetic properties of free cobalt clusters*. Phys. Rev. Lett., 1991. **66**(23): p. 3052–3055
41. P. Gambardella, A. Dallmeyer, K. Maiti, M. C. Malagoli, W. Eberhardt, K. Kern, and C. Carbone, *Ferromagnetism in one-dimensional monatomic metal chains*. Nature, 2002. **416**: p. 301-304.
42. P. Gambardella, S. Rusponi, M. Veronese, S. S. Dhesi, C. Grazioli, A. Dallmeyer, I. Cabria, R. Zeller, P. H. Dederichs, K. Kern, C. Carbone, H. Brune, *Giant Magnetic Anisotropy of Single Cobalt Atoms and Nanoparticles* Science, 2003. **300**(5622): p. 1130-1133.
43. http://www.webelements.com/cobalt/crystal_structure_pdb.html.
44. Guan Ming Wang, Joseph J. BelBruno, Steven D. Kenny, and Roger Smith, *Interaction of silver adatoms and dimers with graphite surfaces* Surf. Sci., 2003. **541**(1-3): p. 91-100.
45. P. Krüger, A. Rakotomahevitra, J. C. Parlebas, and C. Demangeat, *Magnetism of epitaxial 3d-transition-metal monolayers on graphite*. Phys. Rev. B, 1998. **57**(9): p. 5276–5280
46. C. Binns, S. H. Baker, C. Demangeat, and J. C. Parlebas, *Growth, electronic, magnetic and spectroscopic properties of transition metals on graphite* Surf. Sci. Rep., 1999. **34**(4-5): p. 107-170.
47. Johannes V. Barth, Giovanni Costantini, and Klaus Kern, *Engineering atomic and molecular nanostructures at surfaces*. Nature, 2005. **437**: p. 671-679
48. G. Feng, Sebastiaan van Dijken, J. F. Feng, J. M. D. Coey, T. Leo, and David J. Smith, *Annealing of CoFeB/MgO based single and double barrier magnetic tunnel junctions: Tunnel magnetoresistance, bias dependence, and output voltage* J. Appl. Phys., 2009. **105**(033916): p. 1-7.

Appendix A - Spatial Mapping of Inverse Decay Length

$$\kappa(V) = \sqrt{\frac{2m}{\hbar^2} \left(\frac{\Phi_t + \Phi_s}{2} - E + \frac{e|V|}{2} \right) + k_{||}^2} \quad (A1)$$

Assume that $E = 0$ assumed because surface Fermi level in STM is set as zero, and $k_{||} = 17 \text{ nm}^{-1}$; then Eq. A1 will become Eq. A2.

$$\kappa(V) = \sqrt{\frac{m}{\hbar^2} (\Phi_t + \Phi_s) + \frac{m}{\hbar^2} e|V| + (17 \text{ nm}^{-1})^2} \quad (A2)$$

If $C_1 = \frac{m}{\hbar^2} (\Phi_t + \Phi_s)$ and $C_2 = \frac{m}{\hbar^2} e|V|$,

then

$$C_1 = \frac{9.1 \times 10^{-31} \text{ kg} \times (5.2 + 4.6) \text{ eV} \times 1.6 \times 10^{-19} \frac{\text{J}}{\text{eV}}}{(6.626 \times 10^{-34} \text{ J} \cdot \text{s})^2}$$

$$C_1 = \frac{9.1 \times 10^{-31} \text{ kg} \times 9.8 \times 1.6 \times 10^{-19}}{4.39 \times 10^{-67} \frac{\text{kg} \cdot \text{m}^2}{\text{s}^2} \cdot \text{s}^2} = 3.25 \times 10^{18} \text{ m}^{-2} = 3.25 \text{ nm}^{-2}$$

for $V = 0.5 \text{ V}$, then

$$C_2 = \frac{9.1 \times 10^{-31} \text{ kg} \times (0.5) \text{ eV} \times 1.6 \times 10^{-19} \frac{\text{J}}{\text{eV}}}{(6.626 \times 10^{-34} \text{ J} \cdot \text{s})^2} = 0.166 \text{ nm}^{-2}$$

$$\kappa = \sqrt{(3.25 + 0.166 + 289) \text{ nm}^{-2}} = 17.1 \text{ nm}^{-1}$$

So, for graphite, even if we fill all the parameters in Eq. A2 with below numbers (in SI unit) the $k_{||} = K$ will only result $\kappa(V)$ equals to 17 nm^{-1} since the other constants are too small.

$$m = 9.1 \times 10^{-31} \text{ kg}$$

$$\hbar = 6.626 \times 10^{-34} \text{ J} \cdot \text{s}$$

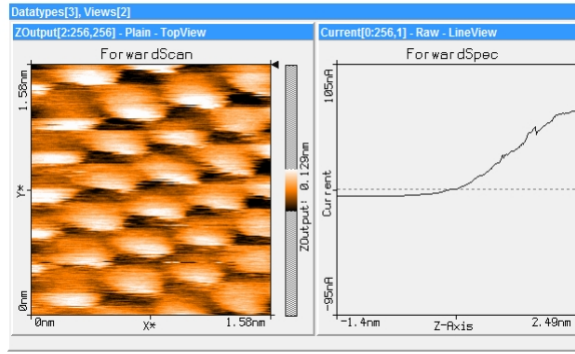
$$\Phi_t = \text{work function of PtIr tip} = 5.2 \text{ eV}$$

$$\Phi_s = \text{the work function of HOPG substrate} = 4.6 \text{ eV}$$

$$1 \text{ eV} = 1.6 \times 10^{-19} \text{ J}$$

For the experimental part, Fig. A1 below is the example of the I - z spectroscopy taken at 0.05 V and -0.05 V . The measurement were taken at fixed current set-point 1 nA . Then the voltage was varied from -0.5 V to 0.5 V with steps of 0.05 V . The I - z spectroscopy were measured several times and at least three best curves at each bias point were selected. From Simmon's model in Eq. 4 the slope $-2k$ can be extracted.

A



B

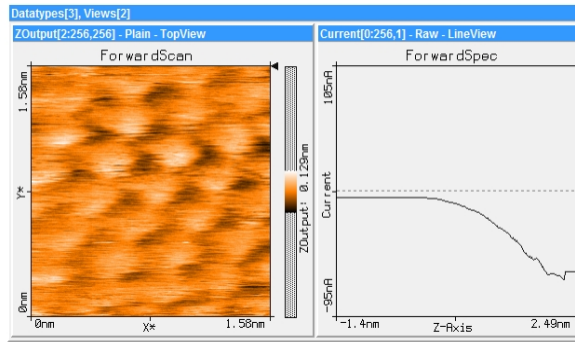


Figure A1. An example of I - z spectroscopy result at current setpoint 1 nA (a) $V = 0.05$ V. (b) $V = -0.05$ V.

The table A1 contained the results of κ versus V for both upper bound and experimental values. Noticed that in the experiment result, the κ is much lower due to smaller $k_{||}$ and present of disorder.

V (Volt)	$K_{\text{upper bound}}$ (nm^{-1})	$K_{\text{experiment}}$ (nm^{-1})
-0.5	17.091	2.461
-0.45	17.091	2.397
-0.4	17.092	2.259
-0.35	17.092	2.352
-0.3	17.092	2.450
-0.25	17.093	2.363
-0.2	17.093	2.358
-0.15	17.094	2.319
-0.1	17.094	2.245
-0.05	17.095	1.352
0.05	17.096	1.088
0.1	17.096	1.434
0.15	17.097	1.384
0.2	17.097	1.523
0.25	17.098	1.618
0.3	17.098	1.656
0.35	17.099	1.729
0.4	17.099	1.777
0.45	17.100	1.770
0.5	17.100	1.765

Table A1. Both theoretical and experimental result of κ versus V for plot in Chapter 4.1.